Extended main sequence turn-off originated from a broad range of stellar rotational velocities

Beomdu Lim[1,2,*] **Gregor Rauw**[1]**, Yaël Nazé**[1]**, Hwankyung Sung**[2]**, Narae Hwang**[3]**, and Byeong-Gon Park**[3,4]

[1]Space sciences, Technologies and Astrophysics Research (STAR) Institute, Université de Liège, Quartier Agora, Allée du 6 Août 19c, Bât. B5C, 4000, Liège, Belgium
[2]Department of Physics and Astronomy, Sejong University, 209 Neungdong-ro, Gwangjin-gu, Seoul 05006, Republic of Korea
[3]School of Space Research, Kyung Hee University, 1732 Deogyeong-daero, Giheung-gu, Yongin-si, Gyeonggi-do 17104, Republic of Korea
[4]Korea Astronomy and Space Science Institute, 776 Daedeokdae-ro, Yuseong-gu, Daejeon 34055, Republic of Korea
[5]Astronomy and Space Science Major, University of Science and Technology, 217 Gajeong-ro, Yuseong-gu, Daejeon 34113, Republic of Korea

*Corresponding author (blim@uliege.be)

Star clusters have long been considered to comprise a simple stellar population, but this paradigm is being challenged, since apart from multiple populations in Galactic globular clusters[1,2], a number of intermediate-age star clusters exhibit a significant colour spread at the main sequence turn-off (MSTO)[3,4,5,6,7,8,9,10,11]. A sequential evolution of multiple generations of stars formed over 100-200 million years is a natural explanation of this colour spread[12]. Another approach to explain this feature is to introduce the effect of stellar rotation[13]. However, its effectiveness has not yet been proven due to the lack of direct measurements of rotational velocities. Here we report the distribution of projected rotational velocities ($V \sin i$) of stars in the Galactic open cluster M11, measured through a Fourier transform analysis. Cluster members display a broad $V \sin i$ distribution, and fast rotators including Be stars have redder colours than slow rotators. Monte Carlo simulations infer that cluster members have highly aligned spin axes and a broad distribution of equatorial velocities biased towards high velocities. Our findings demonstrate how stellar rotation affects the colours of cluster members, suggesting that the colour spread observed in populous clusters can be understood in the context of stellar evolution even without introducing multiple stellar populations.

The total mass of star clusters ranges from about $10^2 M_\odot$ to $\sim 10^6 M_\odot$ (Ref. 14). The minimum initial cluster mass required to retain material ejected from the first generation of stars is about $10^4 M_\odot$ (Ref. 15), and therefore most open clusters ($< 10^4 M_\odot$) are expected to have had insufficient initial mass to host multiple generations of stars with different abundances. This is confirmed by the fact that many open clusters show a negligible variation in terms of chemical composition[16,17] among cluster members. But surprisingly, a colour spread of stars at the MSTO, the so-called "extended MSTO" feature, similar to the one discovered in populous clusters of the Magellanic Clouds (MCs)[3,4,5,6,7,8,9], was found in the Hyades and Praesepe[10,11] open clusters. The suspicion therefore remains of the presence of multiple populations in open clusters. However, stellar rotation has also been advanced to explain the existence of an extended MSTO, and it is important to determine which explanation is correct. To this aim, Galactic

open clusters would be ideal testbeds because their proximity permits the precise derivation of stellar properties, necessary to clarify the origin of the extended MSTO.

M11 is an intermediate-age cluster (250 Myr) at 2 kpc distance[18], having a total mass up to 11000 $M_\odot$ (Refs. 19 and 20). Red clump stars in the cluster show a slight enhancement of α-elements with respect to the solar abundance, but they have a homogeneous chemical composition[20,21,22]. Fig. 1 shows the colour-magnitude diagram of stars in the cluster region (see Methods). In contrast to the narrow distribution in V of the subgiant branch stars, the cluster members near the MSTO ($V = 12.5$ mag) are spread over a wide colour range of 0.3 mag. Given the narrower main sequence band in the fainter regime, photometric errors and a high binary fraction cannot explain the observed spread near the MSTO. If the age spread scenario[12] is applied to the MSTO, the observed colour spread corresponds to an age spread of about 150 Myr. This age spread is comparable to those found in populous clusters in the MCs[3,4,5,7,9,12].

We analyzed high-resolution optical spectra of 164 cluster members near the MSTO obtained from *Gaia*-European Southern Observatory (ESO) Public Spectroscopic Survey internal Data Release 4[23,24] and from observations with *Hectochelle* on the 6.5m Multiple Mirror Telescope (see Methods for details). The red spectra of 164 stars covering the Hα line were used to identify Be stars, while blue spectra of 108 stars containing several weak metallic lines as well as the main spectral line Mg II λ4481 were used in the determination of $V \sin i$.

The presence of rapidly rotating stars in populous clusters of the MCs were inferred through the identification of Be stars[25,26] either from Hα photometry or from limited spectroscopy due to their large distance. But, it remains to be seen whether their colours are different from those of slow rotators or not. In this work, we identified a total of 22 Be stars in M11 by visually inspecting the Hα line profile (Supplementary Fig. 1). Their Hα emission line was found to have a double-peaked shell profile, which is indicative of absorption by a circumstellar disc along the line of sight. We directly measured $V \sin i$ of 108 stars, including the identified Be stars, with available blue spectra by applying a Fourier transform technique[27] to the Mg II λ4481 line for $V \sin i \geq 25$ km s^{-1}, or to the other metallic lines for slower rotators (see Methods for further explanation).

Fig. 2 compares the colours and $V \sin i$ of cluster members. The distribution of very fast rotators ($V \sin i > 200$ km s^{-1}) is extended towards redder colours, while the distribution of slow rotators is shifted towards bluer colours (Fig. 2b). Fig 2c further shows the correlation between the two measurements with a correlation coefficient of about 44 per cent. According to this correlation, a rotating star with $V \sin i = 300$ km s^{-1} has a $U - V$ colour 0.15 mag redder than a non-rotating star. This finding suggests that stellar rotation plays a significant role in the colour spread at the MSTO. We also confirmed that Be stars in M11 are indeed rapidly rotating stars (see also Supplementary Fig. 2) and tend to have colours redder than those of slowly rotating stars.

Rotational mixing plays a similar role to that of convective overshooting in the mixing of internal material. Fresh hydrogen is supplied to the core through the mixing process, and therefore the main sequence lifetime of a rotating star is prolonged by $15 - 62$ per cent for a given mass and metallicity[28]. If cluster members have a broad distribution of rotational velocities, the main sequence band is expected to broaden in colour-magnitude diagrams due to their different main sequence lifetimes. Fast rotation also deforms the shape of a star, lowering the equatorial temperature and luminosity as the equator expands. This gravity darkening effect causes spreads in both magnitude and colour, depending on the inclination angles of spin axes with respect to an observer. In order to test the impact of rotation on the colour-magnitude diagram of the cluster members, the underlying distributions of equatorial velocities (V_{eq}) and inclination angles (i) need to be constrained. We introduced four combinations of V_{eq} and i

distributions to infer their underlying distributions. Case 1 considers a uniform distribution of V_{eq} and a uniform orientation of i in a three-dimensional (3D) space, Case 2 treats a uniform distribution of V_{eq} and a Gaussian distribution of i, Case 3 adopts a linear distribution of V_{eq} and a uniform orientation of i in a 3D space, and Case 4 uses a linear distribution of V_{eq} and a Gaussian distribution of i (see Methods for details). There is no free parameter for Case 1; a peak inclination angle (i_{peak}) and a dispersion (σ_i) are the free parameters to be determined for Case 2; for Case 3, the slope (α) of the linear distribution is the only free parameter; the free parameters i_{peak}, σ_i, and α are required to obtain the distributions of V_{eq} and i for Case 4. We derived those free parameters by comparing the distribution of the observed $V \sin i$ to that of the simulated $V \sin i$ based on the chosen V_{eq} and i distributions (see Methods for further explanation, Supplementary Table 1).

Fig. 3. displays the cumulative distributions of both the observed and simulated $V \sin i$. Case 1 simulations yielded distributions very different from the observed one since the mean probability that the observed distribution is drawn from the simulated case is only about 6.2 ± 4.0 (s.d.) per cent according to the Kolmogorov-Smirnov (K-S) test. Adopting the best-fit parameters ($i_{peak} = 54°$ and $\sigma_i = 1°$), Case 2 simulations reproduce the observed $V \sin i$ distribution with a mean confidence level of 42.1 ± 13.2 per cent. For Case 3, we found a best-fit parameter of $\alpha = 0.0006$ km^{-1} s, however the similarity of the two distributions is only about 10.7 ± 4.6 per cent. Finally, Case 4 simulations yield the best match to the observed distribution with a mean confidence level of 74.1 ± 12.8 per cent; the derived parameters i_{peak}, σ_i, and α are $50°$, $2°$, and 0.0013 km^{-1} s, respectively. This result means that the best-fit distribution of i is a Gaussian distribution centered on $50°$ with a sigma of only $2°$: that implies a strong alignment of spin axes. If the collapsing molecular cloud is rotating, and if it has a rotational kinetic energy comparable to the turbulent kinetic energy, the spin axes of stars formed in the cloud can be aligned. The gravitational interaction among cluster members does not significantly change the spin axes, and therefore the spin alignment can remain for several billion years[29]. The strong alignment of spin axes in M11 can be understood in this context. In addition, the derived slope of the linear distribution of V_{eq} indicates that cluster members may have a distribution of V_{eq} biased towards high rotational velocities, rather than a uniform distribution.

Adopting the V_{eq} and i distributions inferred from Case 4 simulations, a synthetic cluster was generated by taking into account rotational velocity, gravity darkening, the photometric errors of the used data[18], the observed differential reddening[18], and a minimum binary fraction of 5 per cent (see Methods for further explanation). The colour-magnitude diagram of M11 and the synthetic cluster are compared in Fig. 4, demonstrating the similarity between these clusters (especially the colour-rotation spread). In our simulation (Case 4), gravity darkening impacts effective temperature and luminosity by 1.5 ± 0.4 and 7.6 ± 3.4 per cent, respectively, on average, which correspond to impacts of only -0.021 ± 0.006 mag on the $U - V$ colours and -0.080 ± 0.035 on the bolometric magnitude for an A0-type star (Supplementary Fig. 3). On the other hand, the differential reddening in M11 accounts for 0.03 mag (1σ) in $B - V$[18], which corresponds to 0.05 mag (1σ) in $U - V$ according to the usual reddening law[30]. Since the mean $U - V$ photometric error is about 0.02 mag and the total spread is about 0.07 mag (1σ), the colour spread due to the rotation is about 0.05 mag $\left(\sigma_{rot} = \sqrt{\sigma_{obs}^2 - \sigma_{red}^2 - \sigma_{err}^2} \right)$: differential reddening and rotation thus have comparable effect on the $U - V$ colour spread.

Our findings thus indicate that the observed extended MSTO can result from a broad distribution of stellar rotational velocities and does not require the presence of multiple populations. The absence of subgiant branch stars connecting to the red hook of the MSTO also strongly supports a single stellar population scenario for M11 as seen in the populous cluster NGC 1651[10]. The direct comparison between the colours and $V \sin i$ of Be stars proved that their reddened colours are due to fast rotation. This conclusion should certainly be extended to the

populous clusters in the MCs. Our discovery finally challenges ideas about cluster evolution as such clusters were often considered as young counterparts of globular clusters, which comprise multiple populations[1,2], incompatible with our result.

References

1. Hesser, J. E., Hartwick, F. D. A. & McClure, R. D. Cyanogen strengths and ultraviolet excesses of evolved stars in 17 globular clusters from DDO photometry. *Astrophys. J. Suppl. Ser.* **33,** 471-493 (1977)

2. Milone, A. P. *et al.* Multiple Stellar Populations in 47 Tucanae. *Astrophys. J.* **744,** 58-79 (2012)

3. Bertelli, G. *et al.* Testing intermediate-age stellar evolution models with VLT photometry of Large Magellanic Cloud clusters. III. Padova results. *Astron. J.* **125,** 770-784 (2003).

4. Mackey, A. D. & Nielsen, P. B. A double main-sequence turn-off in the rich star cluster NGC 1846 in the Large Magellanic Cloud. *Mon. Not. R. Astron. Soc.* **379,** 151-158 (2007)

5. Goudfrooij, P. *et al.* Population parameters of intermediate-age star clusters in the Large Magellanic Cloud. II. New insights from extended main-sequence turnoff in seven star clusters. *Astrophys. J.* **737,** 3-20 (2011)

6. Girardi, L. *et al.* An extended main-sequence turn-off in the Small Magellanic Cloud star cluster NGC 411. *Mon. Not. R. Astron. Soc.* **431,** 3501-3509 (2013)

7. Li, C., de Grijs, R. & Deng, L. Not-so-simple stellar populations in the intermediate-age Large Magellanic Cloud star clusters NGC 1831 and NGC 1868. *Astrophys. J.* **784,** 157-169 (2014)

8. Li, C., de Grijs, R. & Deng, L. The exclusion of a significant range of ages in a massive star cluster. *Nature* **516,** 367-369 (2014)

9. Milone, A. P. *et al.* Multiple stellar populations in Magellanic Cloud clusters - III. The first evidence of an extended main sequence turn-off in a young cluster: NGC 1856. *Mon. Not. R. Astron. Soc.* **450,** 3750-3764 (2015)

10. Eggen, O. J. The age range of Hyades stars. *Astron. J.* **116,** 284-292 (1998)

11. Brandt, T. D. & Huang, C. X. The age and age spread of the Praesepe and Hyades clusters: A consistent, $\sim$800 Myr picture from rotating stellar models. *Astrophys. J.* **807,** 24-29 (2015)

12. Goudfrooij, P. *et al.* Population parameters of intermediate-age star clusters in the Large Magellanic Cloud. I. NGC 1846 and its wide main-sequence turnoff. *Astron. J.* **137,** 4988-5002 (2009)

13. Bastian, N. & de Mink, S. E. The effect of stellar rotation on colour–magnitude diagrams: on the apparent presence of multiple populations in intermediate age stellar clusters. *Mon. Not. R. Astron. Soc.* **398,** L11–L15 (2009).

14. Turner, J. L. Extreme Star Formation. *Astrophysics and Space Science Proceedings* 10, 215 (2009). 1009.1416.

15. Conroy, C. & Spergel, D. N. On the formation of multiple stellar populations in globular clusters. *Astrophys. J.* **726,** 36-48 (2011)

16. Pancino, E. *et al.* Chemical abundance analysis of the open clusters Cr 110, NGC 2099 (M 37), NGC 2420, NGC 7789, and M 67 (NGC 2682). *Astron. Astrophys.* **511,** 56-74 (2010)

17. Reddy, A. B. S., Giridhar, S. & Lambert, D. L. Comprehensive abundance analysis of red giants in the open clusters NGC 2527, 2682, 2482, 2539, 2335, 2251 and 2266. *Mon. Not. R. Astron. Soc.* **431,** 3338-3348 (2013)

18. Sung, H. *et al. UBVI* CCD photometry of M11 - II. New photometry and surface density profiles, *Mon. Not. R. Astron. Soc.* **310**, 982-1001 (1999)

19. Santos Jr. J. F. C., Bonatto, C. & Bica, E. Structure and stellar content analysis of the open cluster M 11 with 2MASS photometry. *Astron. Astrophys.* **442,** 201-209 (2005)

20. Cantat-Gaudin, T. *et al.* The Gaia-ESO Survey: Stellar content and elemental abundances in the massive cluster NGC 6705. *Astron. Astrophys.* **569,** 17-34 (2014)

21. Magrini, L. *et al.* The Gaia-ESO Survey: Abundance ratios in the inner-disk open clusters Trumpler 20, NGC 4815, NGC 6705. *Astron. Astrophys.* **563,** 44-57 (2014)

22. Tautvaišienė, G. *et al.* The Gaia-ESO Survey: CNO abundances in the open clusters Trumpler 20, NGC 4815, and NGC 6705. *Astron. Astrophys.* **573,** 55-67 (2015)

23. Gilmore, G. *et al.* The Gaia-ESO Public Spectroscopic Survey, *The Messenger* **147**, 25-31 (2012)

24. Randich, S., Gilmore, G., & Gaia-ESO Consortium. The Gaia-ESO Large Public Spectroscopic Survey, *The Messenger* **514**, 47-49 (2013)

25. Milone, A. P. *et al.* Multiple stellar populations in Magellanic Cloud clusters – VI. A survey of multiple sequences and Be stars in young clusters. *Mon. Not. R. Astron. Soc.* **477,** 2640–2663 (2018)

26. Dupree, A. K. *et al.* NGC 1866: First Spectroscopic Detection of Fast-rotating Stars in a Young LMC Cluster. *Astrophys. J. Lett.* **846,** 1-7 (2017)

27. Gray, D. F. *The observation and analysis of stellar photospheres*, **3rd ed.** (Cambridge University Press), 458-504 (2005)

28. Georgy, C. *et al.* Populations of rotating stars I. Models from 1.7 to 15 $M_\odot$ at $Z = 0.014$, 0.006, and 0.002 with $\Omega/\Omega_{\mathrm{cri}}$ between 0 and 1. *Astron. Astrophys.* **553,** 24-40 (2013)

29. Corsaro E. *et al.* Spin alignment of stars in old open clusters, *Nature Astron.* **1**, 0064- (2017)

30. Guetter, H. H. & Vrba, F. J. Reddening and polarimetric studies toward IC 1805. *Astron. J.* **98,** 611-746 (1989)
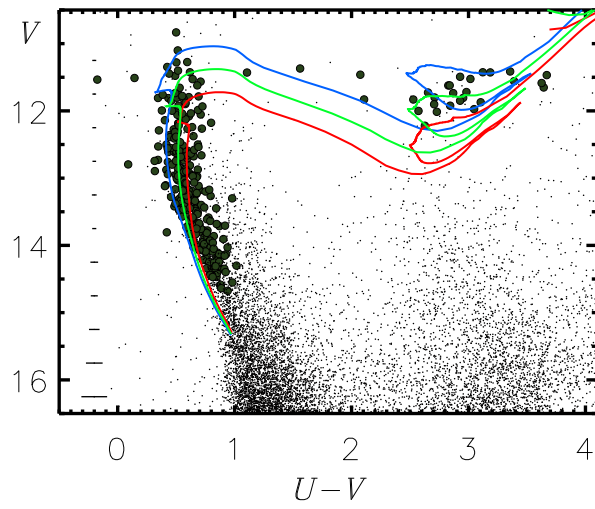
Figure 1: **Colour-magnitude diagram of the Galactic populous cluster M11.** Bold dots represent the cluster members selected from proper motion data. Error bars indicate mean photometric errors within given magnitude bins. Solid lines are isochrones of the Geneva stellar evolution models for the relative angular velocity to the critical value $\omega = 0.7$ and $\log t = 8.4$, 8.5, and 8.6, respectively [yr][28].
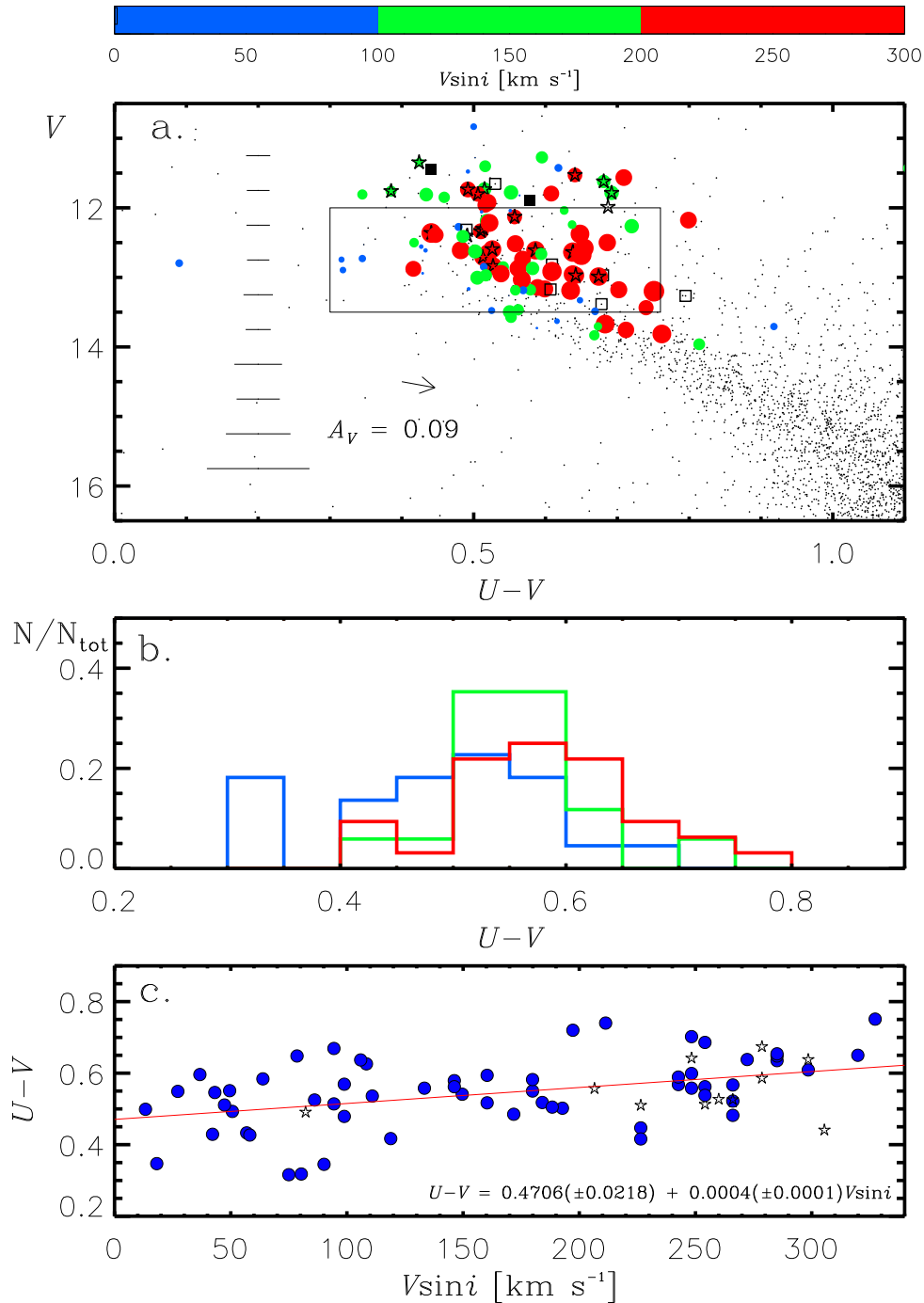
Figure 2: **Correlation between $V\sin i$ and $U - V$ colours. a.** The colour-magnitude diagram of intermediate-mass stars near the MSTO. The size of dots are proportional to $V\sin i$. Star symbols, filled squares, open squares, and small dots represent Be stars, eclipsing binaries, double-lined spectroscopic binary candidates, and the other stars without $V\sin i$ measurement, respectively. Error bars display mean photometric errors within given magnitude bins. **b.** The $U - V$ distributions of stars within the outlined box in panel **a** in three different $V\sin i$ ranges that we used (identified by 3 colours, see the scale bar). Histograms were normalized by the total number of stars within given $V\sin i$ ranges. Note that binary stars were not used in this analysis. **c.** The colour variation with respect to $V\sin i$ for the same sample as used in panel **b**. Be stars are plotted as star symbols. The solid line represents the result of a linear least square regression, and its solution is expressed in the bottom of the panel.
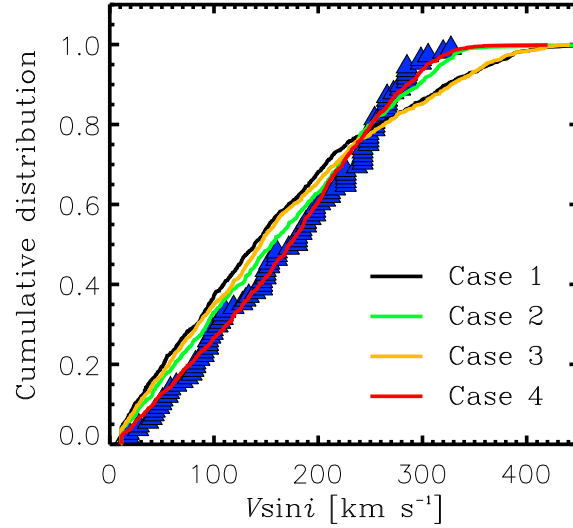
Figure 3: **Cumulative distribution of $V \sin i$ from observations and simulations.** Blue triangles represent the observed $V \sin i$ distribution, while black, green, orange, and red solid lines show the samples from the simulated distributions adopting the best parameters for Cases 1, 2, 3, and 4, respectively.
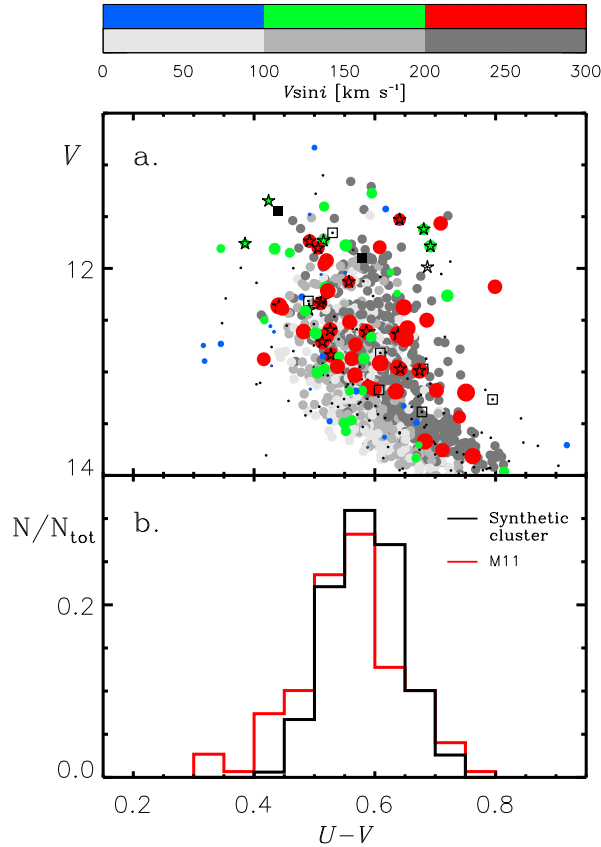
Figure 4: **Comparison of M11 and a synthetic cluster (single population). a.** The $(V, U-V)$ colour-magnitude diagram observed for M11 (coloured dot as in Fig. 1.) and of our synthetic cluster (gray dot, with darken shades indicating faster rotating stars). **b.** Colour distribution of the observed (red) and artificial (black) stars within the same colours and magnitude ranges as outlined in Fig. 2a. Note their very good match.

Methods

Data acquisition. The published[18] UBV photometric data of M11 cover a $40' \times 40'$ region centered on the cluster. Mean photometric errors down to the visual magnitude of 14 mag are about 1% in V magnitude, $V - I$, and $B - V$, and better than 2% in $U - B$. The proper motion of stars allows us to distinguish the bona fide members from field interlopers because the cluster members have almost the same kinematic properties. For this purpose, we used two catalogues of proper motion[31,32] for stars in the M11 field in member selection. The members were selected using the following criteria: 1) membership probabilities higher than 70 per cent from both catalogues[31,32], 2) $B - V$ bluer than 0.62, and 3) visual magnitude brighter than 14 mag. The membership validity was tested using the proper motion data from *Gaia* Data Release 2[33,34]. The proper motions of the stars having counterparts from the *Gaia* catalogue are well constrained within a small kinematic boundary (Supplementary Fig. 4). A total of 277 members near the MSTO were finally included in our target list.

Queue scheduled observations of 37 of these cluster members were carried out on 2017 May 5, 24, and June 9 with the multi-object high-resolution spectrograph Hectochelle[35] attached to the 6.5-m telescope of the MMT observatory. The spectral resolving power of Hectochelle is about $R \sim 34000$. The observations of the stars were made with the order-separating filter OB 25 transmitting light in the wavelength range of 6475Å – 6630Å in a 2×1 binning mode. Dome flat and ThAr lamp spectra were also taken, just before and after the target exposure. Data reduction was made according to the standard procedure for extraction of one dimensional spectra[36,37]. Sky-subtracted spectra were combined into a single spectrum for the same star, and then normalized by using continuum levels found from a cubic spline interpolation.

The high-resolution spectra of 155 cluster members were obtained from the *Gaia*-ESO Public Spectroscopic Survey internal Data Release 4*(Ref. 23 and 24). Note that 28 stars were observed at both the MMT and Paranal observatories. The spectroscopic observations were made with either GIRAFFE ($R \sim 17000 - 26000$)[38] or Ultraviolet and Visual Echelle Spectrograph (UVES, $R \sim 47000$)[39] attached to the 8.2m Very Large Telescope (Unit 2). The red spectra of 155 stars were taken with more than one instrumental setup among GIRAFFE/HR14A, HR15N, and UVES/U580, while the blue spectra of 133 stars were acquired by using either GIRAFFE/HR5A or UVES/U520 setups. The procedures of pre-processing and calibrations were made through their data reduction pipelines (see the ESO Phase 3 Data Release Description† for detail). The flattened, wavelength-corrected, and sky-subtracted spectra of given stars are delivered as the final data. We normalized the reduced spectra using the same method as above.

Binary stars. We found seven double-lined spectroscopic binary candidates from visual inspection of the spectra. Five of them had been identified as spectroscopic binaries using a cross-correlation technique in a previous study of the same data[40]. Since we are studying only 60 per cent of the full sample of cluster members, about a dozen spectroscopic binaries are expected for the full sample. In addition, two eclipsing binary members were found in a previous study[41]. Therefore, the minimum binary fraction among cluster members is about 5 per cent.

Fourier analysis. We used the Fourier technique to determine $V \sin i$ of stars[27]. The profile of a spectral line can be expressed by a convolution of a flux profile with various broadening functions related to stellar rotation, thermal motion, microturbulence, macroturbulence, and

---

*The *Gaia*-ESO public data can be accessed through the link https://www.gaia-eso.eu/data-products/public-data-releases

†http://www.eso.org/rm/api/v1/public/releaseDescriptions/92

instrumental characteristics[27]. The profile of a spectral line is dominated by the rotation profile if the contribution of the rotational broadening is large enough compared to that of the other broadening sources. The rotation-dominated profile have zeros at low frequency in the Fourier space, while the other broadening components do not have zeros. The frequency of the first zero depends on $V \sin i$, having a relation as below:

$$\frac{\lambda}{c} \sigma_1 V \sin i = 0.660 \tag{1}$$

where λ, c, and σ_1 represent the rest-frame wavelength of a given spectral line, the speed of light, and the frequency of the first zero.

Our sample stars are intermediate-mass (late-B to A-type) stars, known to have a broad range of rotational velocities[42,43]. Careful selection of isolated lines is important to obtain reliable $V \sin i$ because spectral lines in their spectra could be easily blended with adjacent lines due to the large rotational broadening. The Mg II doublet at $\lambda 4481$ Å is a moderately strong line which is not much sensitive to temperature. This line is properly separated from adjacent lines, and is therefore the most suitable line to determine $V \sin i$ for rapidly rotating A- to late-B-type stars ($V \sin i > 100$ km s^{-1}). In addition, several weak metallic lines can be used in the $V \sin i$ range of 10 km s^{-1} to 70 km s^{-1}.

The spectra taken with the GIRAFFE/HR5A grating contain Mg II $\lambda 4481$ and a handful of metallic lines around Hγ. UVES spectra contain more metallic lines because of its wide wavelength coverage (Supplementary Table 2). Those additional metallic lines were not blended with adjacent lines and were not seriously affected by the Hγ absorption line[44]. We computed the Fourier transform of these lines and measured the frequency of the first zero[27]. $V \sin i$ derived from Mg II $\lambda 4481$ were compared with those found from the other metallic lines (Supplementary Fig. 5). Since the intrinsic separation between the doublet components of Mg II $\lambda 4481$ dominantly influences the line profile of slow rotators ($V \sin i < 25$ km s^{-1}), the Fourier method overestimate $V \sin i$[44] in that case. We adopted the mean values of $V \sin i$ derived from the other metallic lines as the $V \sin i$ for slow rotators. In other cases, $V \sin i$ derived from Mg II $\lambda 4481$ was consistent with those from the other metallic lines in the $V \sin i$ range of 25 km s^{-1} to 40 km s^{-1}. Fe and Ti lines are blended with adjacent lines in the higher velocity regime ($V \sin i > 70$ km s^{-1}), and thereby yielding higher $V \sin i$ than those from Mg II $\lambda 4481$.

$V \sin i$ could be derived for 108 out of 133 stars with available blue spectra. The spectra of the remaining stars had either insufficient signal-to-noise ratio (SNR) to identify Mg II $\lambda 4481$ or/and metallic emission lines, or they were eclipsing binaries. In addition, a limb darkening coefficient was also estimated to be 0.53 in this procedure from comparison with a pure rotation profile in the Fourier space[43] (Supplementary Fig. 6). This value is in a good agreement with a previous measurement at 4000-4500 Å[45].

Error estimation. We estimated the errors of the measured $V \sin i$ through Monte-Carlo simulations. To this aim, we used synthetic spectra without noise for effective temperatures of 10000 K and 13000 K generated using the spectrum analysis code SPECTRUM v2.76[27] and Kurucz ODFNEW model atmospheres[46]. Rotational broadening functions for various $V \sin i$ from 25 km s^{-1} to 350 km s^{-1} were applied to the synthetic spectra using the AVSINI programme of SPECTRUM, where a limb darkening coefficient of 0.53 was adopted. These spectra were convolved with an instrumental broadening function ($\Delta \lambda = 0.24$Å) using SMOOTH2[27]. We carried out the Fourier transform of Mg II $\lambda 4481$ in the synthetic spectra and compared the derived $V \sin i$ with input values ($V \sin i_{input}$) (Supplementary Fig. 7).

Linear least-square fitting to the difference between $V \sin i$ and $V \sin i_{input}$ ($\Delta V \sin i$) was made in the $V \sin i_{input}$ range of 0 km s^{-1} to 230 km s^{-1}, where the intercept was set to 0 km s^{-1}. We obtained $\Delta V \sin i = 0.03 V \sin i_{input}$. This relation indicated that a systematic error

of about 3 per cent is involved in our measurements. $\Delta V \sin i$ for $V \sin i_{\text{input}} > 230$ km s^{-1} is approximated by the equation $\Delta V \sin i = 0.26(V \sin i_{\text{input}} - 230) + 7.47$. The systematic errors continuously increased up to 11 per cent at 350 km s^{-1} as Mg II $\lambda 4481$ begins to be blended with distant He I $\lambda 4471$ and metallic lines.

Noise corresponding to a given SNR was added to the synthetic spectra adopting $V \sin i$ of 25 km s^{-1} to 350 km s^{-1}, respectively, using the RANDOMU function of IDL, where the SNRs were set from 10 to 100 with an interval of 10 for a given $V \sin i$, respectively. Each simulation was repeated 100 times for the same setup, and the $V \sin i$ were estimated in each case as made above. The standard deviations of the derived $V \sin i$ distributions were adopted as the random errors for a given SNR and $V \sin i$ (Supplementary Fig. 7). The random errors exceeded 50 km s^{-1} only for SNRs lower than 20 and $V \sin i$ in the range 250 km $^{-1}$ to 350 km s^{-1}. Using those simulations, we estimated the random errors of $V \sin i$ for the observed SNRs of our spectra and the derived $V \sin i$ after correcting for the systematic errors. The errors were smaller than 30 km s^{-1} in most cases (Supplementary Fig. 7). The typical random errors for very slow rotators ($V \sin i < 25$ km s^{-1}) was estimated to be about 1.4 km s^{-1} from the standard deviation of their $V \sin i$ measurements.

A- and B-type stars, in general, do not have convective currents in their photospheres, and therefore it is difficult to imagine macroscopic motions such as the solar granules. Nevertheless, measurable radial-tangential macroturbulence (about 5 km s^{-1}) was found in very slowly rotating stars ($V \sin i < 20$ km s^{-1})[47]. Such macroturbulent broadening, together with instrumental broadening, can systematically influence their $V \sin i$ measurements. Our sample contains four very slow rotators ($V \sin i < 25$ km s^{-1}) observed with GIRAFFE/HR5A. Since Mg II $\lambda 4481$ cannot be used for them because of its doublet nature, we analyzed the other metallic lines (Fe I $\lambda 4404$, Fe II $\lambda 4489$ $\lambda 4491$ Ti II $\lambda 4468$, and $\lambda 4488$) to investigate systematic errors and the lower limit of measurable $V \sin i$ for the instrumental setup.

Synthetic spectra without noise were generated using the same method as above, and then broadened by adopting a radial-tangential macroturbulent velocity of 5 km s^{-1} with MAC-TURB[27]. Rotational broadening functions corresponding to $V \sin i$ from 5 km s^{-1} to 25 km s^{-1} were applied to five synthetic spectra, respectively. Each spectrum was finally broadened with SMOOTH2 according to the spectral resolution of GIRAFFE/HR5A. We then derived $V \sin i$ from those Fe and Ti lines. Comparison of the input $V \sin i$ with the measured ones showed the mean difference in the $V \sin i$ range of 10 km s^{-1} to 25 km s^{-1} to be about 1.1 km s^{-1}. This is the systematic error in the $V \sin i$ range. For the input $V \sin i$ of 5 km s^{-1}, the measured $V \sin i$ was overestimated on average by 5.4 km s^{-1}. Therefore, the lower limit of our measurements that are not affected by macroturbulent and instrumental broadening is about 10 km s^{-1}, and all the very slowly rotating stars in our sample have $V \sin i$ higher than the limit.

Underlying distribution of V_{eq} and i. With stellar mass, V_{eq} and i are the key parameters in generating the colour-magnitude diagram of a synthetic cluster. However, the underlying distributions of these parameters for the members of M11 are unknown. Here, we introduce a method to infer these underlying distributions using a Monte-Carlo technique.

A total of 1000 artificial stars were used in each simulation. Given the masses of the stars at the MSTO of M11, stellar masses were generated in the range of $2.4 M_{\odot}$ to $3.6 M_{\odot}$, where the mass function of M11 ($\Gamma = -2.0$)[18] was used as the probability function. Stars can rotate up to a critical velocity (V_{cri}) when the centrifugal force equals the gravitational force, and V_{cri} varies as a function of stellar mass. The maximum V_{eq} of given stars were taken by interpolating their masses to the mass-V_{cri} relation of the Geneva isochrone adopting $\omega = 0.95$ and $\log t = 8.4$ [yr][28]. Individual artificial stars have V_{eq} and i in the ranges of 0 km s^{-1} to V_{cri} and of $0°$ to $90°$, respectively.

We considered four cases for the probability distributions of V_{eq} and i. For V_{eq}, either a uniform distribution or a linear distribution was adopted, while either a uniform orientation in 3D space or a Gaussian distribution was assumed for i. The uniform distribution of V_{eq} means that V_{eq} are evenly generated between 0 km s^{-1} and V_{cri}. The high number fraction of fast rotators ($V \sin i > 200$ km s^{-1}) that we find in M11 may indicate that the underlying distribution of V_{eq} may be biased towards the high velocity regime (Supplementary Fig. 2). We therefore assumed a linear probability distribution following:

$$P(V_{eq}) = \alpha(V_{eq} - 396.18) + 1. \tag{2}$$

where α is the slope of the distribution and a free parameter to be determined in Cases 3 and 4. The probability distribution is normalized at 396.18 km s^{-1} which is the maximum V_{cri} in the Geneva isochrone adopting $\omega = 0.95$ and $\log t = 8.4$ [yr][28]. In addition, a distribution of spin axes uniformly oriented in a 3D space is seen to an observer as a distribution biased towards high i because of projection effect[29]. The probability distribution of i in Cases 1 and 3 is then given by a uniform distribution in $\cos i$. We randomly selected $\cos i$ between 0 and 1 to consider the symmetric behaviour of the cosine function for i larger than 90°. i were obtained from their inverse cosine values.

Recently, a strong alignment of spin axes of stars was found in a few old open clusters[29,48]. This fact allows us to consider a Gaussian probability distribution of i:

$$P(i) = \frac{1}{\sqrt{2\pi\sigma_i^2}} e^{\frac{(i - i_{peak})^2}{2\sigma_i^2}} \tag{3}$$

where the peak inclination angle (i_{peak}) and the dispersion (σ_i) are free parameters to be determined in Cases 2 and 4.

We introduced the systematic and random errors estimated above to the $V \sin i$ of artificial stars. The simulated distributions of $V \sin i$ were then compared with the observed one using the K-S test. This simulation was repeated 1000 times to suppress the statistical fluctuation, and then the resultant probabilities were averaged.

For Cases $2-4$, we tested i_{peak} in the range 5° to 90° (with a step of 5°), σ_i in the range of 1° to 46° (with a step of 5°), and α between 0 km^{-1} s and 0.0023 km^{-1} s (with a step of 0.0005 km^{-1} s). The systematic and random errors were added to the resultant $V \sin i$. The distributions of the simulated $V \sin i$ for each case were then compared with the observed one using the K-S test. This provided the first estimation of each parameter. Refined simulations were then made around the first estimation using 20 per cent smaller steps. As a result, we found the best-fit parameters (Supplementary Figs. 8, 9, and 10).

Gravity darkening effects. We corrected for gravity darkening effects on the temperature and luminosity from the Roche potential model for rotating stars following the description of Ref. 49. A relation between the bolometric luminosity and the luminosity measured by an observer is expressed by Equation 6 of Ref. 49:

$$L(i) = L_{bol} \frac{4}{\Sigma} \int_{d\Sigma \cdot d > 0} f^4(x, \omega, \theta) d\Sigma \cdot d = L_{bol} C_L(i, \omega) \tag{4}$$

where Σ, d, and $C_L(i, \omega)$ are the surface of a star and the direction of the observer inclined by i from its spin axis, and the geometric correction term in luminosity, respectively. On the other hand, the effective temperature inferred by an observer can be obtained by averaging flux over the projected surface (Σ_p) of a star. The relation between the mean effective temperature and

the observed temperature is given by Equation 9 of Ref. 49 as below:

$$T_{\text{eff}}(i,\omega) = T_{\text{eff,mean}} \left[\frac{1}{\Sigma_p} \int_{d\Sigma \cdot d > 0} f^4(x,\omega,\theta) d\Sigma \cdot d \right]^{\frac{1}{4}} = T_{\text{eff,mean}} C_{T_{\text{eff}}}(i,\omega) \tag{5}$$

where $C_{T_{\text{eff}}}(i,\omega)$ is the geometric correction term on the effective temperature. The geometric correction terms for luminosity and effective temperature were computed for 21 values of i from $0°$ to $90°$ with an interval of $4.5°$ and for 21 values of ω ranging from 0.0 to 1 with an interval of 0.05, respectively (Supplementary Fig. 3).

A synthetic colour-magnitude diagram. We assigned masses, V_{eq}, and i to 1000 artificial stars based on the mass function[18] and the probability distributions from the Case 4 simulation. The other parameters of the artificial stars, such as effective temperature, bolometric luminosity, pole radius (R_p), and oblateness, were obtained by interpolating their mass and V_{eq} to a grid of the Geneva isochrones ($\log t = 8.4$) in the ω range of 0 to 0.95[28].

The critical velocities of given artificial stars were computed by using the equation below:

$$V_{\text{cri}} = \sqrt{\frac{GM}{R_{\text{eq}}}} = \sqrt{\frac{2GM}{3R_p}} \tag{6}$$

Their ω were computed according to the equation $\omega = \frac{3}{2} \frac{V_{\text{eq}}}{V_{\text{cri}}} \frac{R_p}{R_{\text{eq}}}$. The gravity darkening correction values were obtained by interpolating the grids of the geometric correction values [$C_L(i,\omega)$ and $C_{T_{\text{eff}}}(i,\omega)$] according to the values of i and ω and then applied to the effective temperature and bolometric luminosity of the individual artificial stars, respectively.

The corrected effective temperature and luminosity were transformed to $U - V$ and M_V using a colour-temperature relation and bolometric correction for the solar metallicity[50]. A distance modulus ($V - M_V$) of 11.55 mag and mean reddening $E(U - V)$ of 0.74 from a previous study[18] were applied to the synthetic colour-magnitude diagram. Non-negligible differential reddening was found in M11[18]: $E(B - V)$ ranges from 0.38 to 0.48 mag with a standard deviation of 0.03 mag, which corresponds to 0.05 mag in $E(U - V)$. The differential reddening was randomly introduced to the synthetic colour-magnitude diagram assuming a Gaussian distribution with the standard deviation. The photometric errors in $U - V$ and V provided from the published data[18] were averaged within each V magnitude bin of 1 mag. These mean errors were adopted as the dispersions of the Gaussian distributions. Photometric errors generated from these distributions were added to the synthetic colour-magnitude diagram. About 50 stars were brightened by 0.75 mag adopting the minimum binary fraction of 5 per cent. We found that the adopted $U - V$ colour scale[50] appears to be, on average, about 0.05 bluer than the one[51] used in the reddening determination of the previous study[18] (see Supplementary Fig. 11). The $U - V$ colours of the artificial stars were thus shifted by such a systematic difference.

Data Availability. In this paper, we use publicly available data : photometry from Ref. 18, evolutionary tracks from the Geneva stellar evolution group (Ref. 28, `https://www.unige.ch/sciences/astro/evolution/en/?lang=en`), astrometry from *Gaia* DR2 (`https://www.cosmos.esa.int/gaia`), and spectra from *Gaia*-ESO survey (`https://www.gaia-eso.eu/data-products/public-data-releases`). New MMT Hα spectra (shown in Supplementary Fig. 1) and derived $V \sin i$ (used in Figs 2, 3, 4 , and Supplementary. Fig. 2) are available for download at `ftp://ftp.astro.ulg.ac.be/pub/users/lim` (anonymous ftp).

References

31. McNamara, B. J., Pratt, N. M., & Sanders, W. L. Membership in the open cluster M11, *Astron. Astrophys. Suppl.* **27,** 117-143 (1977)

32. Su, C.-G., Zhao, J.-L., & Tian, K.-P. Membership determination of stars using proper motions in the region of the open cluster M 11, *Astron. Astrophys. Suppl.* **128,** 255-264 (1998)

33. Gaia Collaboration *et al.* The Gaia mission. *Astron. Astrophys.* **595,** 1-36 (2016)

34. Gaia Collaboration *et al.* Gaia Data Release 2. Summary of the contents and survey properties. *eprint arXiv:1804.09365* (2018)

35. Szentgyorgyi, A. *et al.* Hectochelle: A Multiobject Optical Echelle Spectrograph for the MMT, *Publ. Astron. Soc. Pac.* **123**, 1188-1209 (2011)

36. Lim, B. *et al.* A Constraint on the Formation Timescale of the Young Open Cluster NGC 2264: Lithium Abundance of Pre-main Sequence Stars. *Astrophys. J.* **831,** 116-133 (2016)

37. Lim, B. *et al.* Kinematic evidence for feedback-driven star formation in NGC 1893. *Mon. Not. R. Astron. Soc.* **477,** 1993-2003 (2018)

38. Pasquini, L. *et al.* Installation and commissioning of FLAMES, the VLT Multifibre Facility. *The Messenger* **110**, 1-9 (2002)

39. Dekker, H. *et al.* Design, construction, and performance of UVES, the echelle spectrograph for the UT2 Kueyen Telescope at the ESO Paranal Observatory. in *SPIE Proceedings: Optical and IR Telescope Instrumentation and Detectors.* 534-545 (2000)

40. Merle, T. *et al.* The Gaia-ESO Survey: double-, triple-, and quadruple-line spectroscopic binary candidates, *Astron. Astrophys.* **608**, 95-128 (2017)

41. Koo, J.-R. *et al.* Variable Stars in the Open Cluster M11 (NGC 6705). *Publ. Astron. Soc. Pac.* **119,** 1233-1246 (2007)

42. Brown, A. G. A., & Verschueren, W. High S/N Echelle spectroscopy in young stellar groups II. Rotational velocities of early-type stars in Sco OB2, *Astron. Astrophys.* **319**, 811-838 (1997)

43. Royer, F., Zorec, J., & Gómez, A. E. Rotational velocities of A-type stars III. Velocity distributions, *Astron. Astrophys.* **463**, 671-582 (2007)

44. Royer, F., Gerbaldi, M., Faraggiana, R., & Gómez, A. E. Rotational velocities of A-type stars I. Measurement of $v \sin i$ in the southern hemisphere, *Astron. Astrophys.* **381**, 105-121 (2002)

45. Al-Naimiy, H. M. Linearized limb-darkening coefficients for use in analysis of eclipsing binary light curves. *Astrophys. Sp. Sci.* **53,** 181-192 (1978)

46. Castelli, F. & Kurucz, R. L. New Grids of ATLAS9 Model Atmospheres. *eprint arXiv:astro-ph/0405087* (2004).

47. Gray, D. Precise Rotation Rates for Five Slowly Rotating a Stars. *Astron. J.* **147,** 81-93 (2014)

48. Kovacs, G. Signature of non-isotropic distribution of stellar rotation inclination angles in the Praesepe cluster. *Astron. Astrophys.* **612,** 2-6 (2018)

49. Georgy, C. *et al.* Populations of rotating stars III. SYCLIST, the new Geneva population synthesis code. *Astron. Astrophys.* **566,** 21-35 (2014)

50. Worthey, G. & Lee, H.-C. An Empirical UBV RI JHK Color-Temperature Calibration for Stars. *Astrophys. J. Suppl. Ser.* **193,** 1-11 (2011)

51. Mermilliod, J.-C. Comparative studies of young open clusters. III - Empirical isochronous curves and the zero age main sequence. *Astron. Astrophys.* **97,** 235-244 (1981)

Acknowledgements

Author Contributions
BL proposed this project, analyzed the data, and wrote the manuscript. GR computed the gravity darkening effects. YN developed the Fourier transform code. HS was involved in the planning the project. All co-authors participated in discussion and contributed to improvement of the manuscript.

Competing Interests
The authors declare that they have no competing financial interests.

Correspondence
Correspondence and requests for materials should be addressed to Beomdu Lim (email:blim@uliege.be).
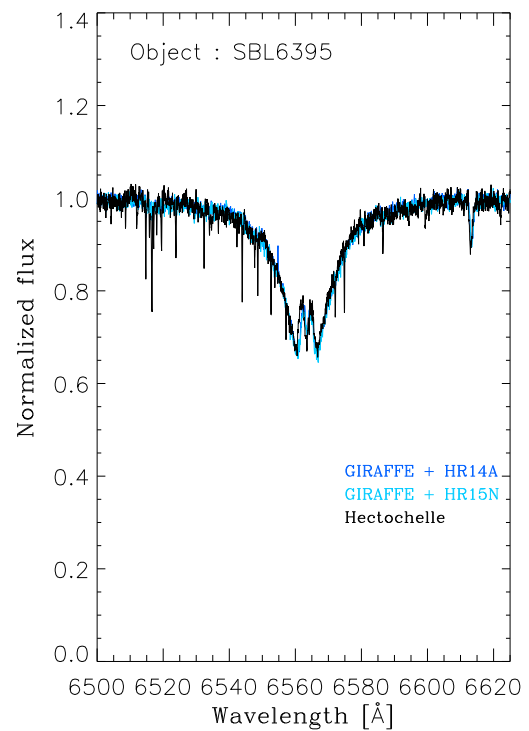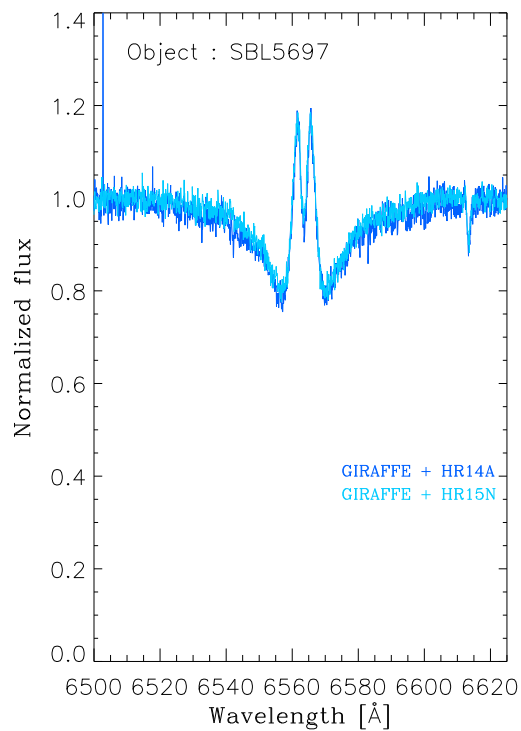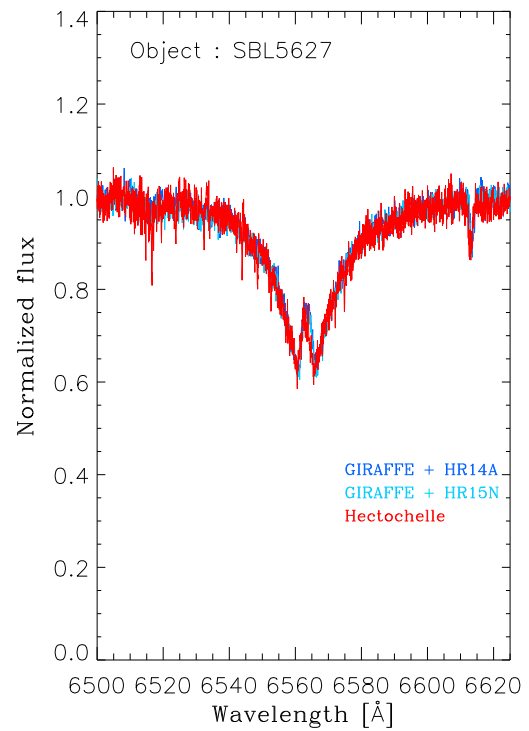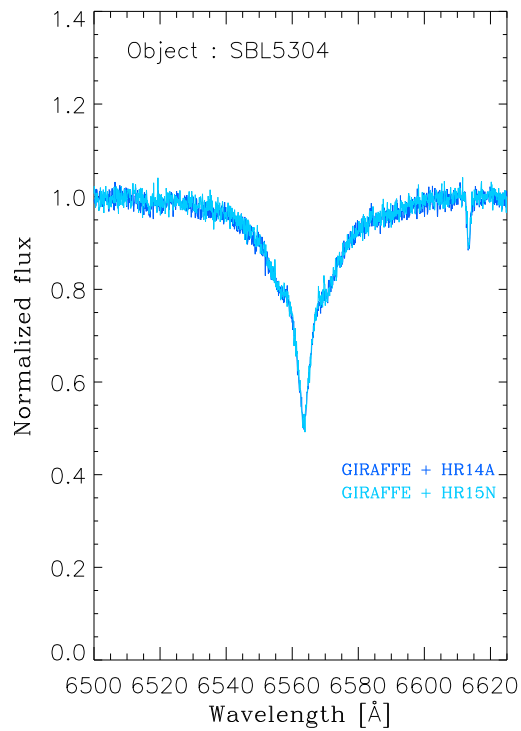
Supplementary Figure 1: **Hα emission line of Be stars.** These spectra were taken from three different spectrographs FLAMES/GIRAFFE (blue and cyan), UVES (green), and Hectochelle (black, yellow green, and red).
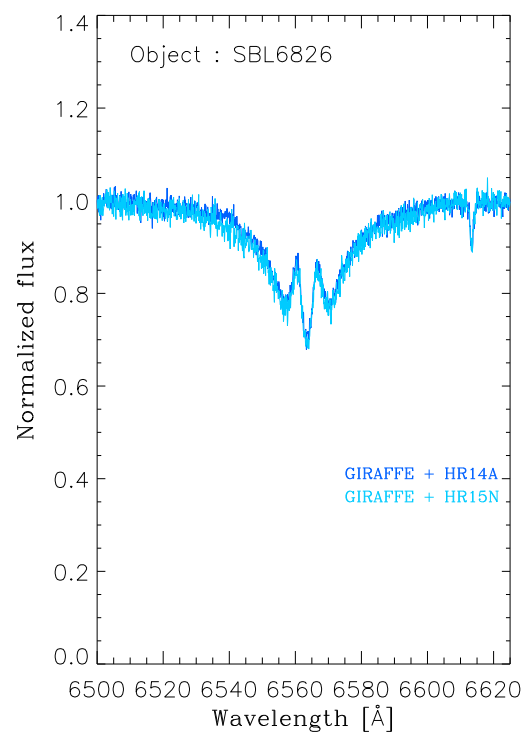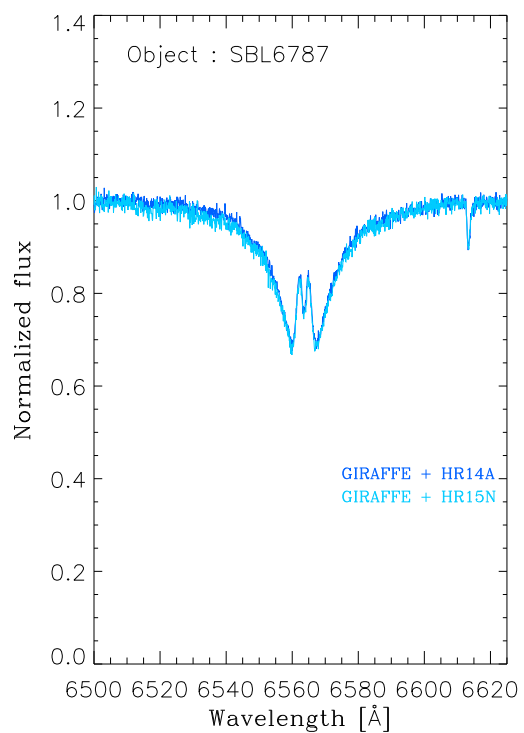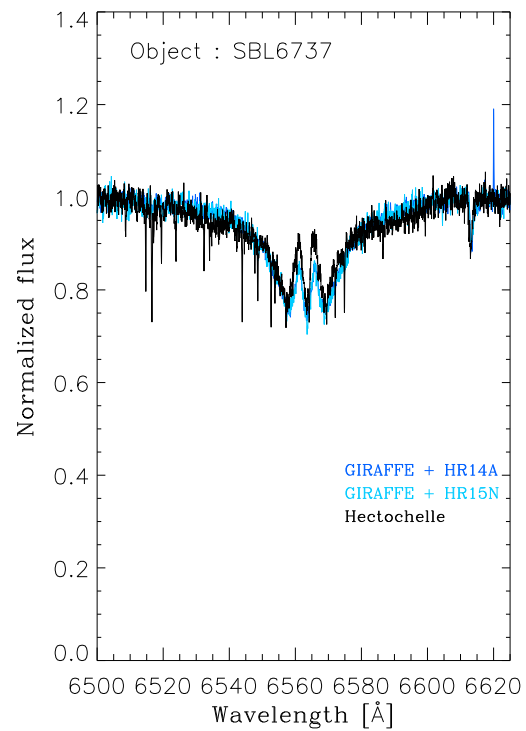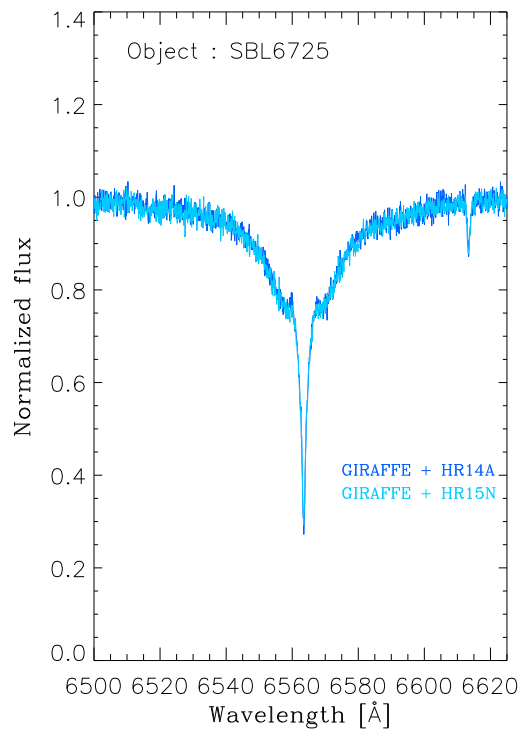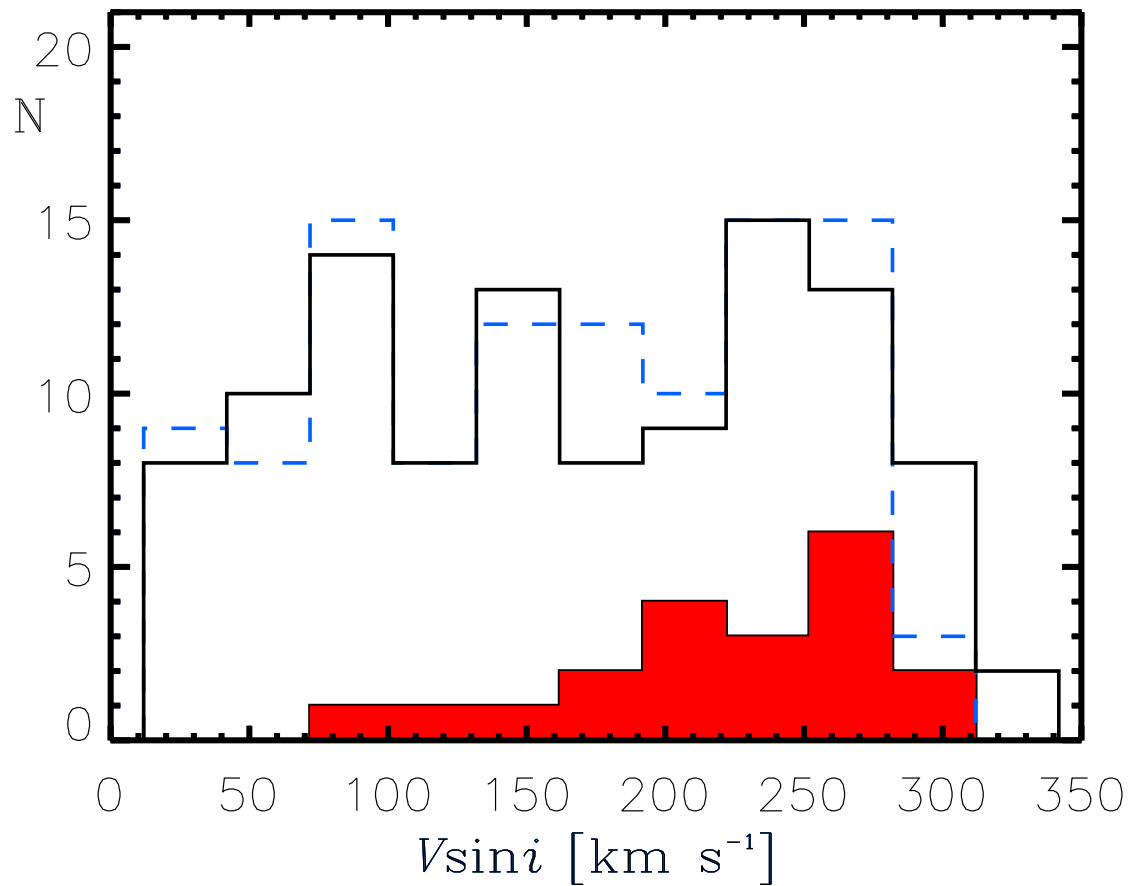
Supplementary Figure 1: (Continue)
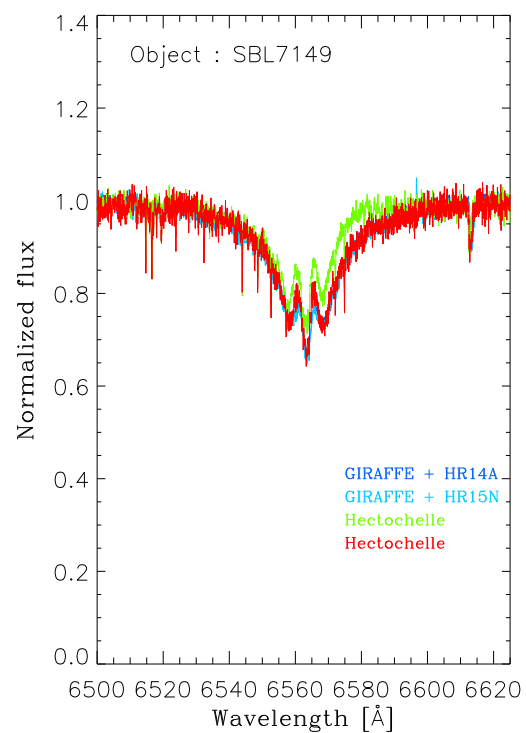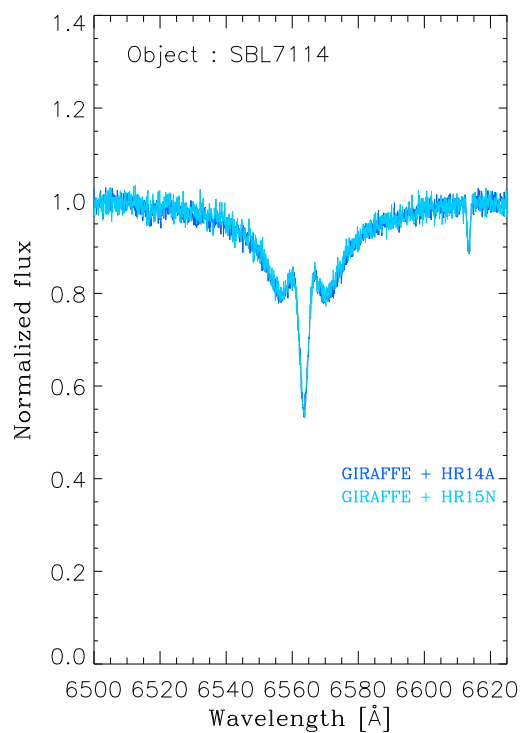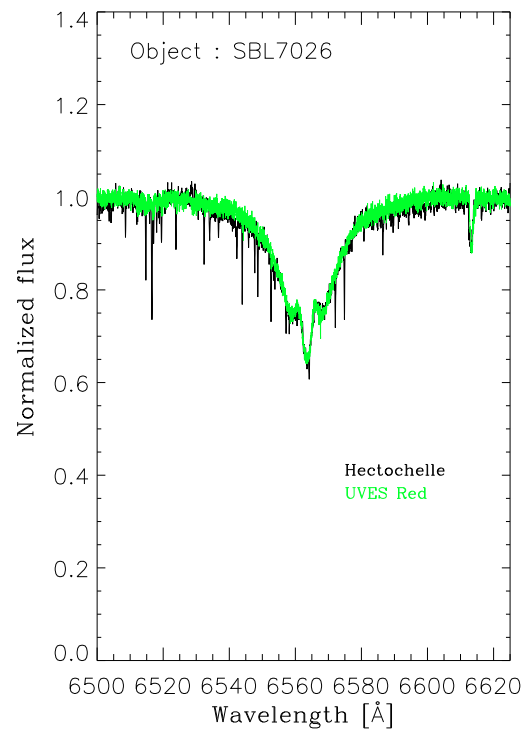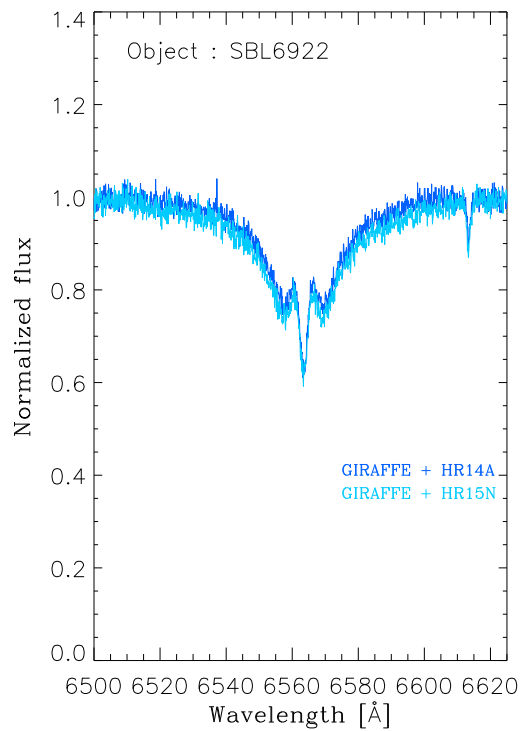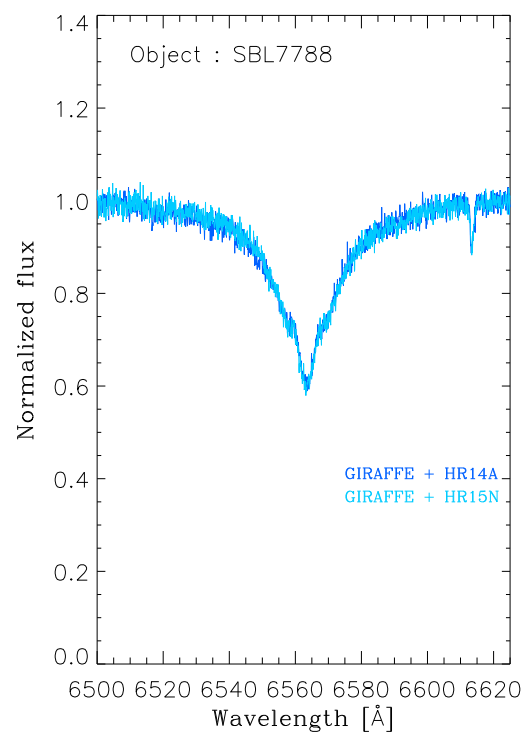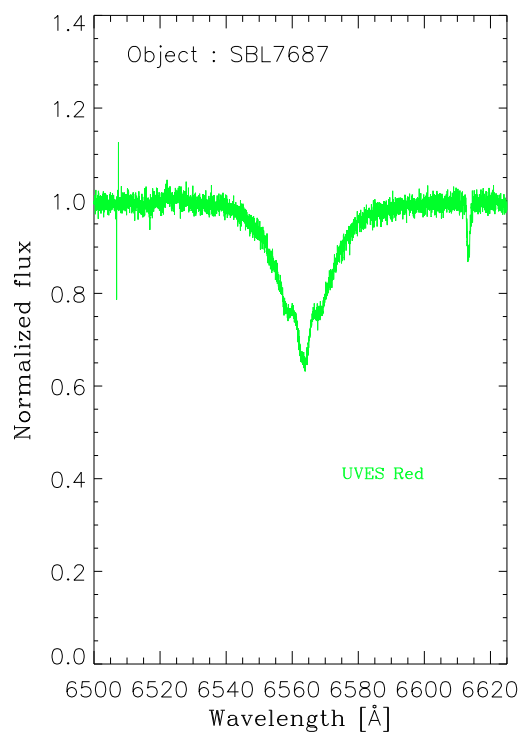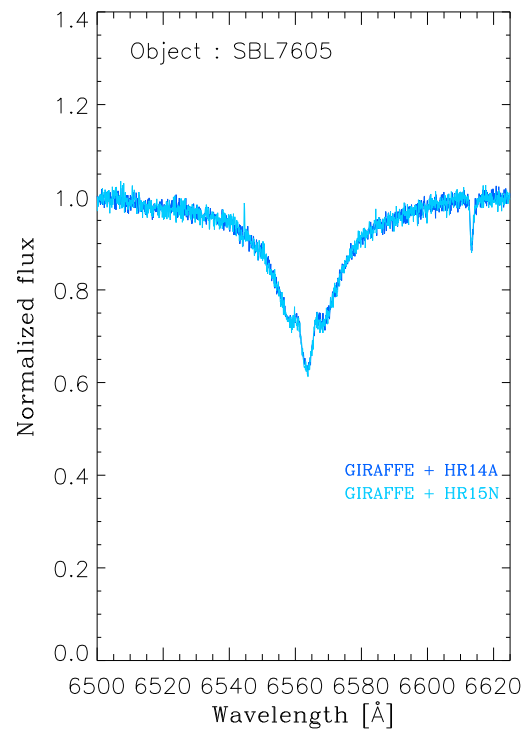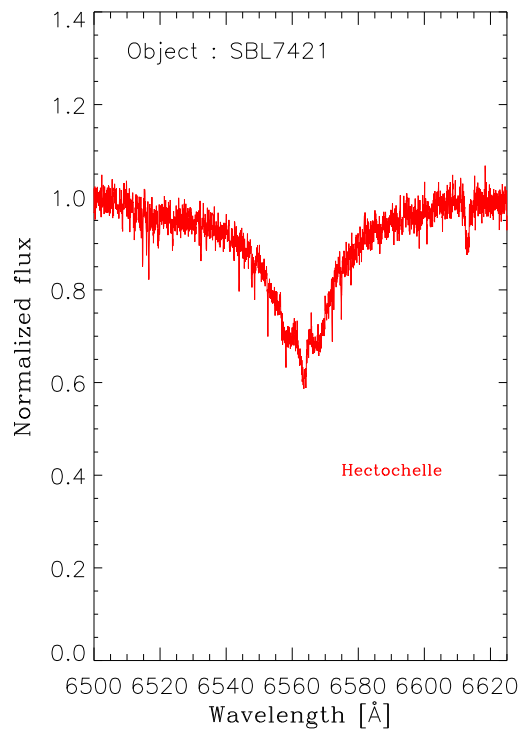
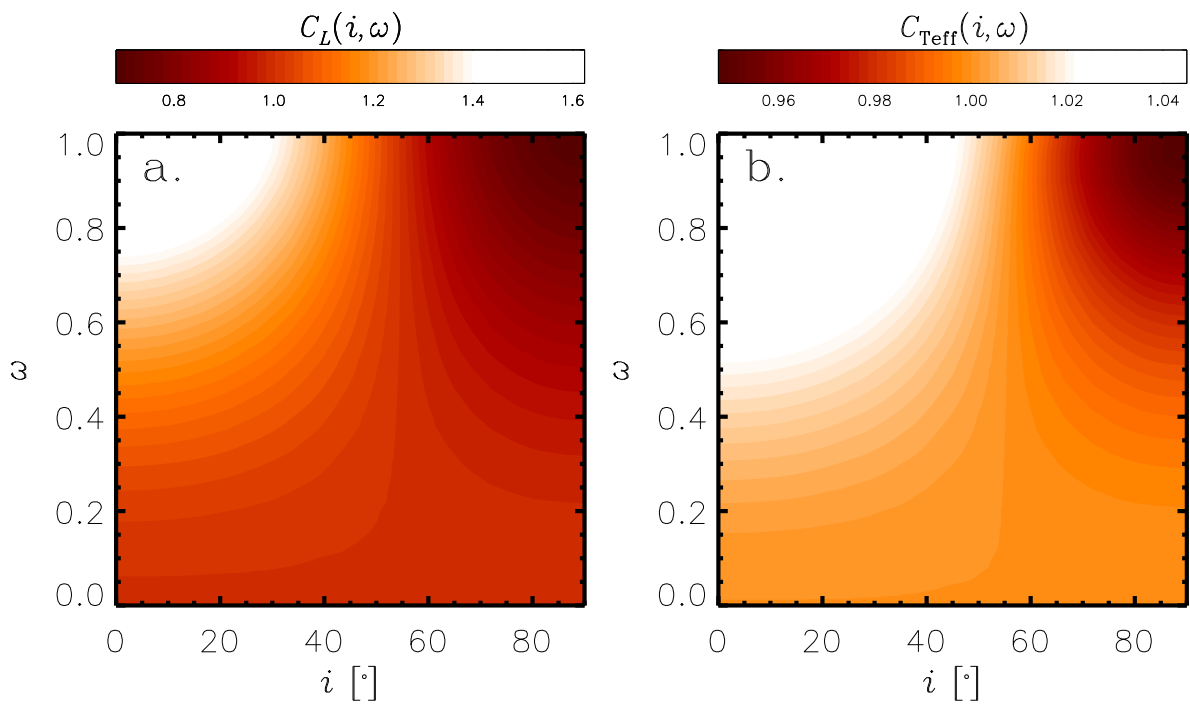Supplementary Figure 1: (Continue)
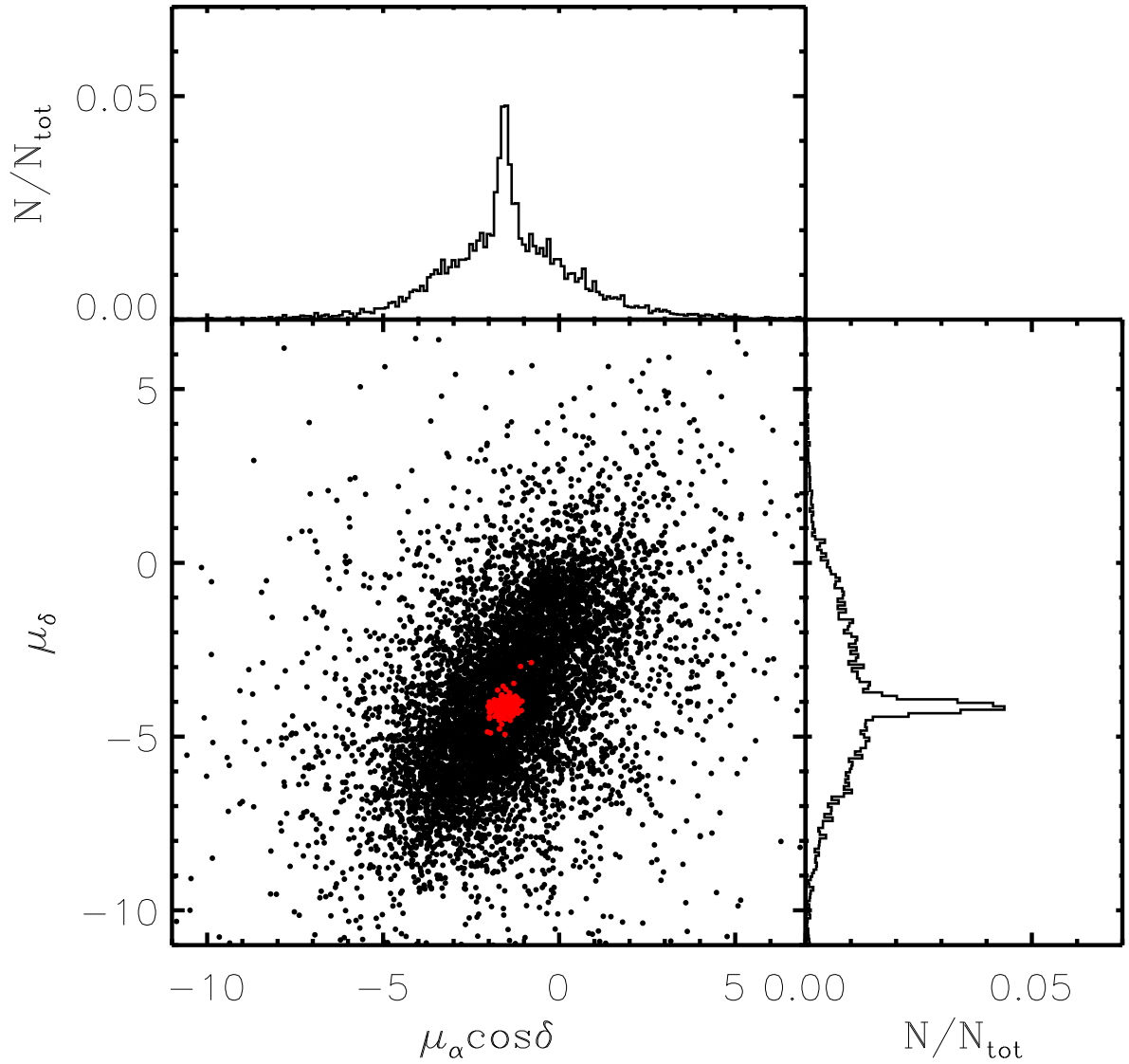
Supplementary Figure 1: (Continue)
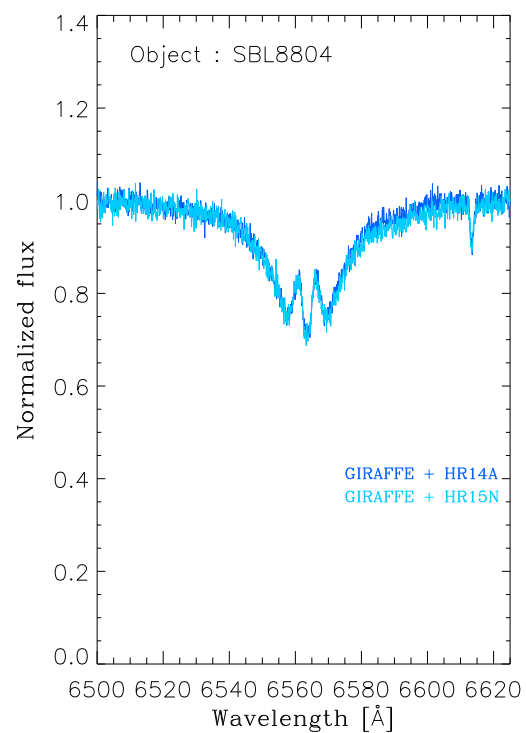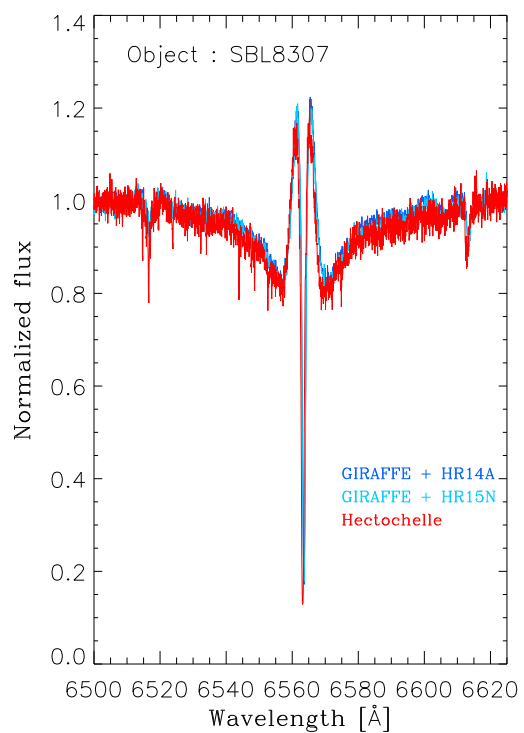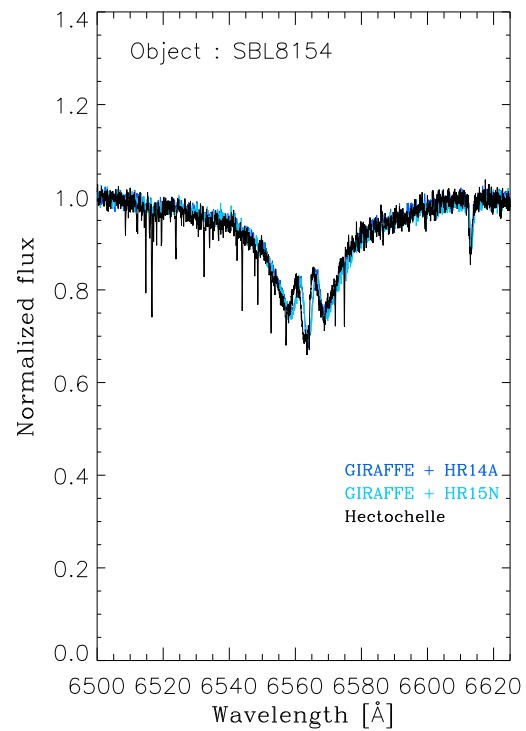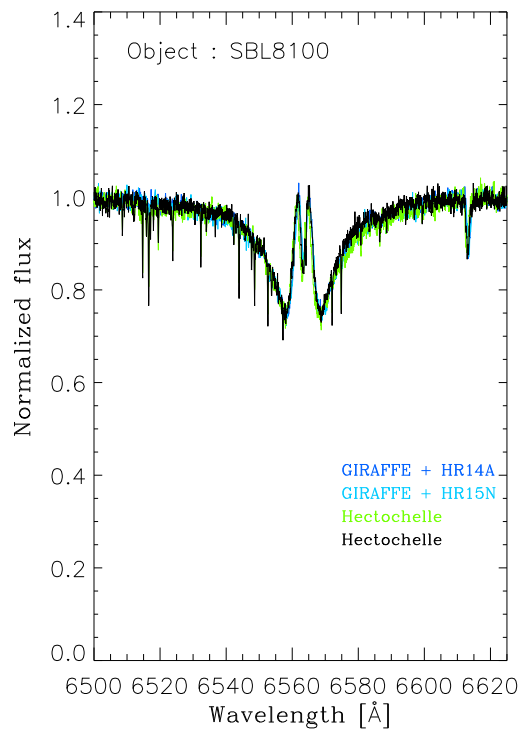
Supplementary Figure 1: (Continue)
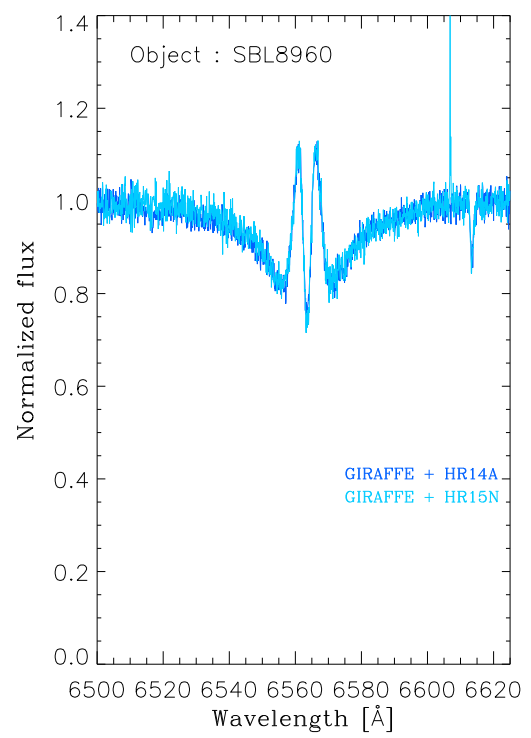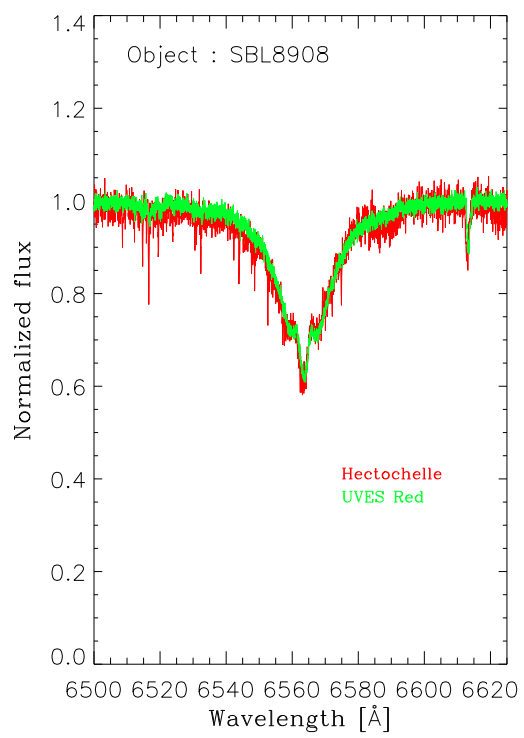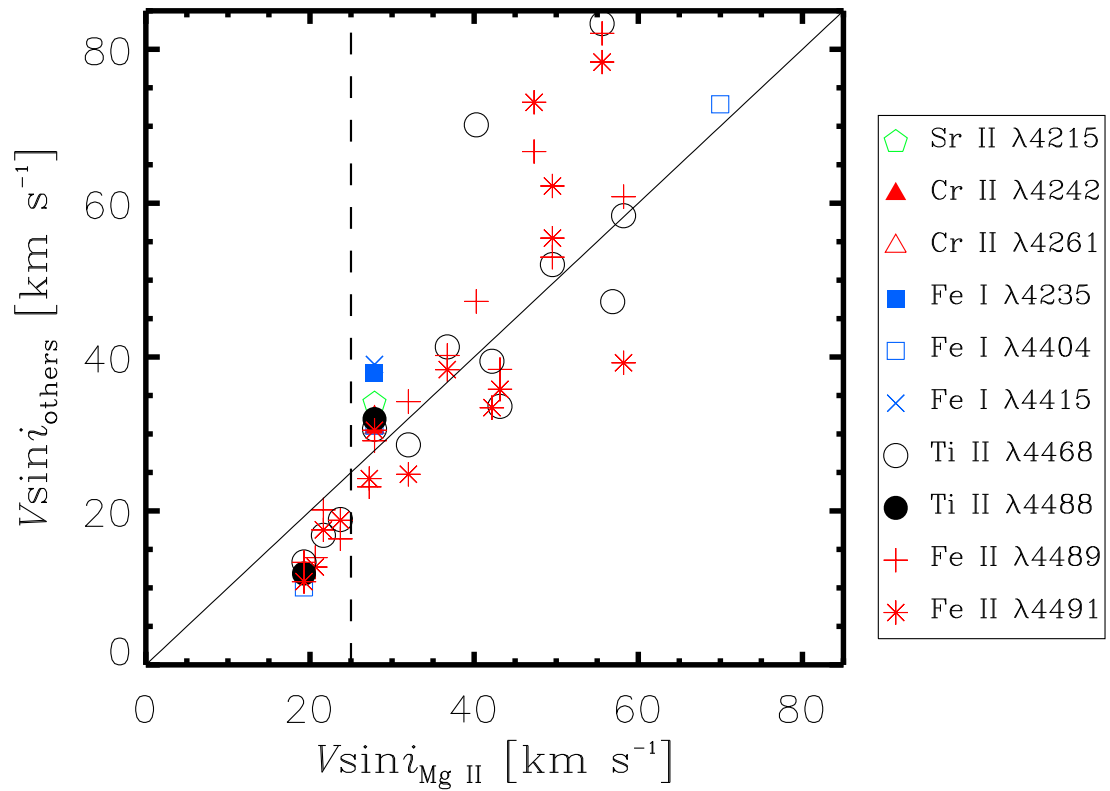
Supplementary Figure 1: (Continue)

Supplementary Figure 2: **Distribution of** $V \sin i$. Solid and dashed line histograms represent the distributions of the observed $V \sin i$ and the systematic error-corrected $V \sin i$, respectively. The red histogram shows the $V \sin i$ distribution of Be stars. All the histograms were obtained with a bin size of 30 km s^{-1}.

Supplementary Figure 3: **Gravity darkening effects on luminosity and effective temperature. a.** The geometric correction term for luminosity with respect to *i* and *ω*. **b.** The geometric correction term for effective temperature. The correction values were plotted on a linear scale.

Supplementary Figure 4: **Distribution of proper motion of stars from Gaia Data Release 2**[33,34]. Black dots are all the stars observed by Gaia in the M11 field, while red dots are the members selected from previous proper motion data[31,32]. Histograms were obtained along each proper motion direction.

Supplementary Figure 5: **Comparison of** $V \sin i$ **derived from Mg** II $\lambda 4481$ **with those from the other metallic lines.** Solid line represents the one-to-one correspondence of two measurements. Dashed line denotes the lower limit of measurable $V \sin i$ from the Mg II $\lambda 4481$ line.
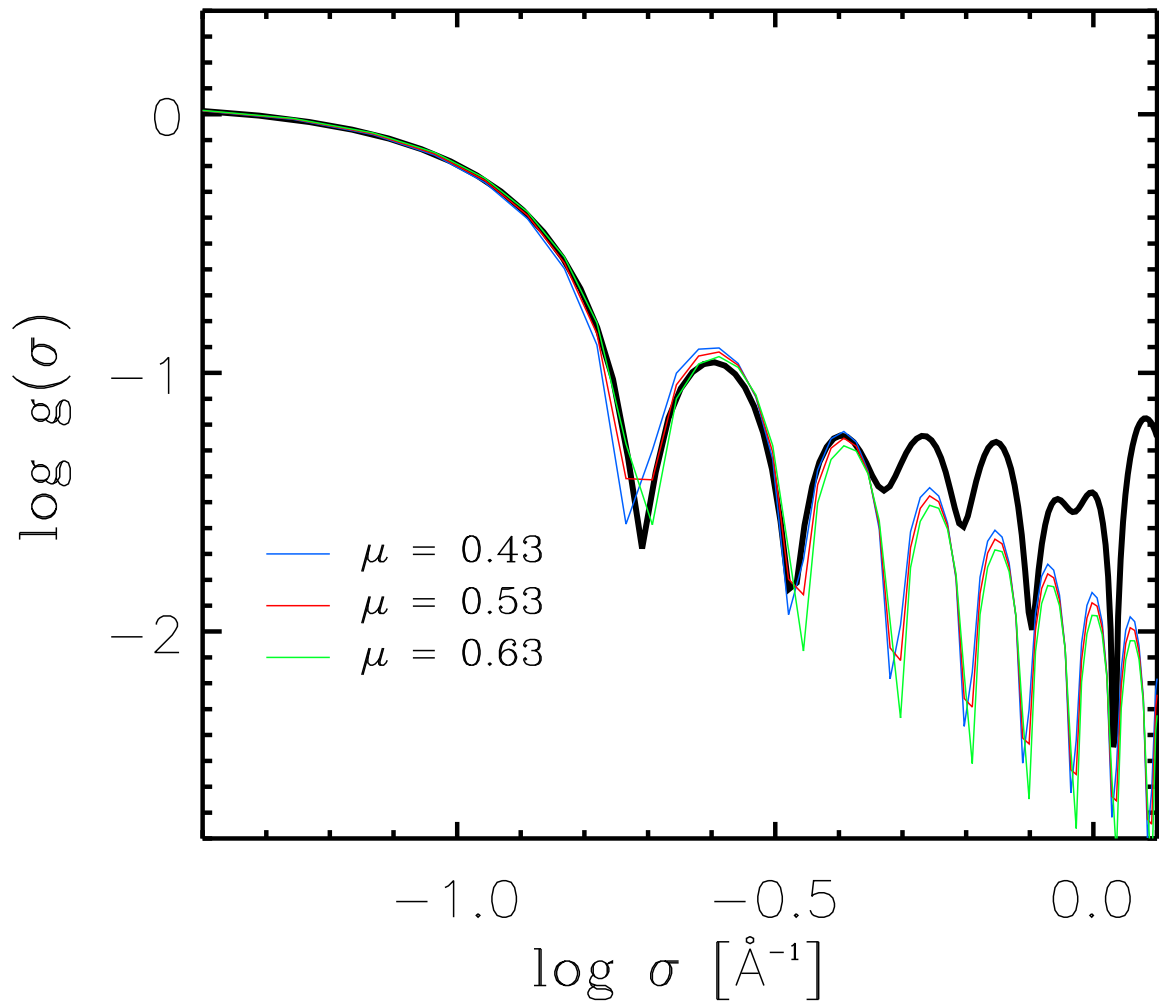
Supplementary Figure 6: **Fourier spectrum of the Mg ɪɪ λ4481 line for a star in our sample (thick solid line).** The thin solid line represents the Fourier spectra of a pure rotation profile adopting different limb darkening coefficients, respectively.
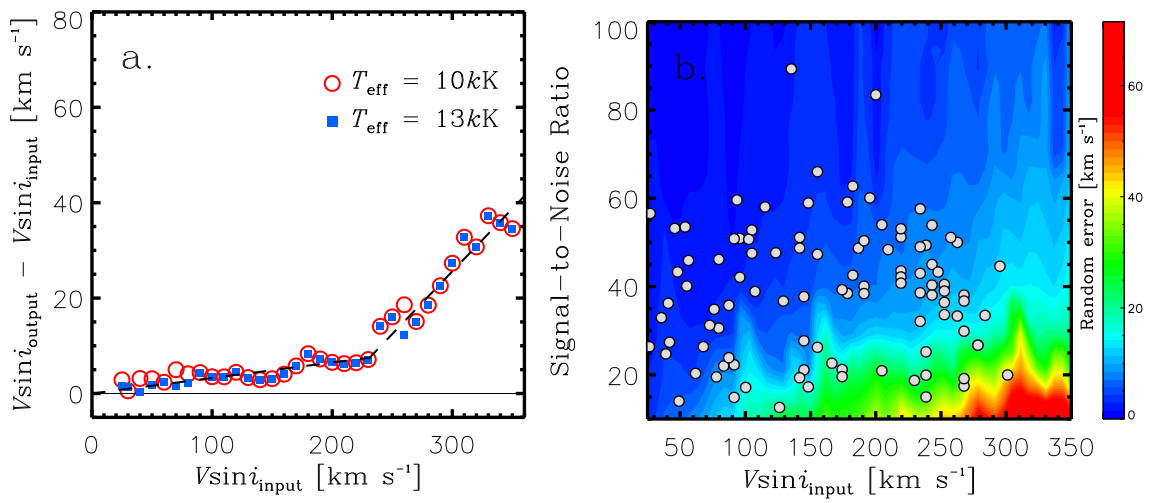
Supplementary Figure 7: **Estimation of measurement errors. a.** Systematic errors as a function of input $V\sin i$. The systematic errors involved in $V\sin i$ are not affected by effective temperature. Dashed lines show the results from linear least-square fitting to the systematic difference. **b.** Distribution of random errors with respect to input $V\sin i$ and SNR. Dots in the right panel denote the systematic error-corrected $V\sin i$ of observed stars and the SNRs of their spectra.
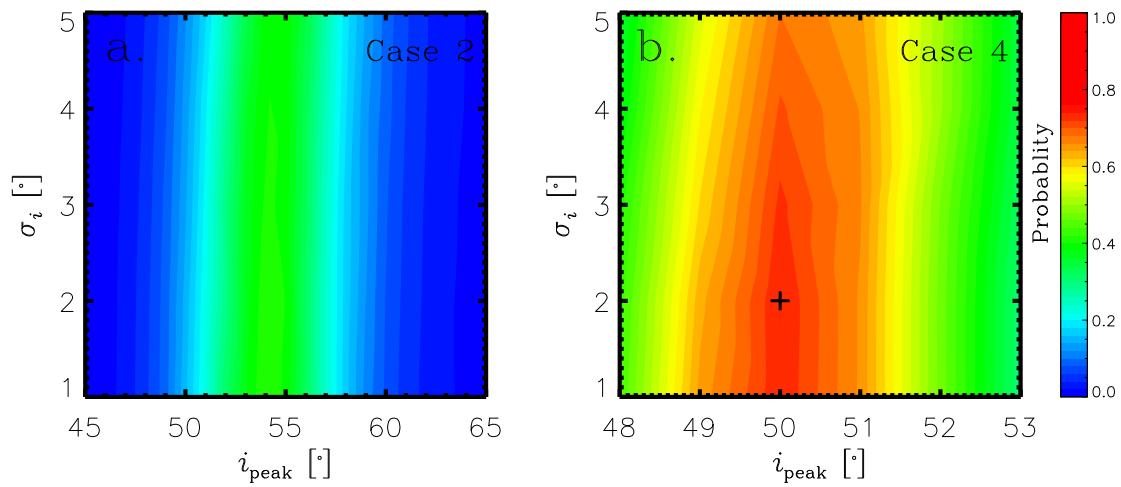
Supplementary Figure 8: **Probability distributions with respect to i_{peak} and σ_i.** The contours shows the distribution of mean probabilities obtained from 1000 times simulations for each case, where the probabilities were computed with the K-S test between $V\sin i$ distributions for simulations and observations. **a.** Parameter space for the Case 2 simulations. The mean probabilities appears high between $50°$ and $53°$. However, a specific value of σ_i cannot be well constrained because the mean probabilities are almost the same in the range of $1°$ to $5°$. **b.** Parameter space for the Case 4 simulation. The cross indicates i_{peak} and σ_i showing highest probability with which to properly reproduce the observed $V\sin i$.
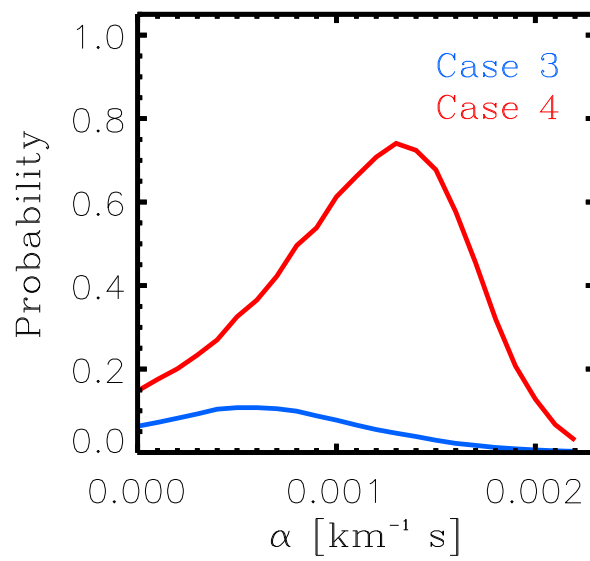
Supplementary Figure 9: **Probability distributions with respect to α.** Blue and red solid lines represent the variation of the mean probabilities from the K-S test for the Cases 3 and 4 simulations, respectively.
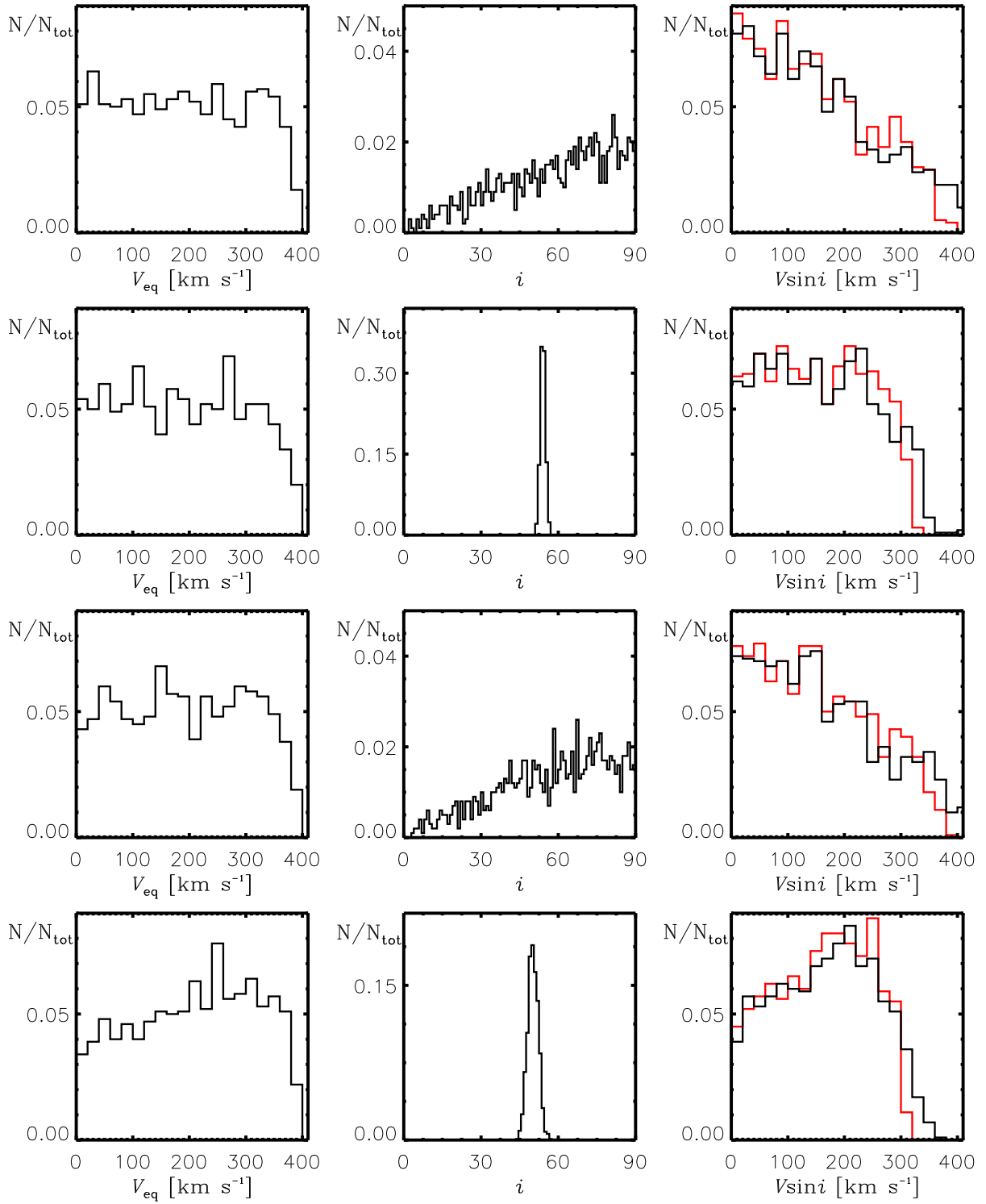
Supplementary Figure 10: **Examples of underlying distributions inferred from each simulation.** Left-hand, middle, and right-hand panels show the distributions of V_{eq}, i, and $V \sin i$, respectively. In the right-hand panels, red histograms represent the distributions of the simulated $V \sin i$, while black histograms display those of the error-added $V \sin i$. The examples generated for Cases 1 to 4 are plotted from top to bottom, respectively.
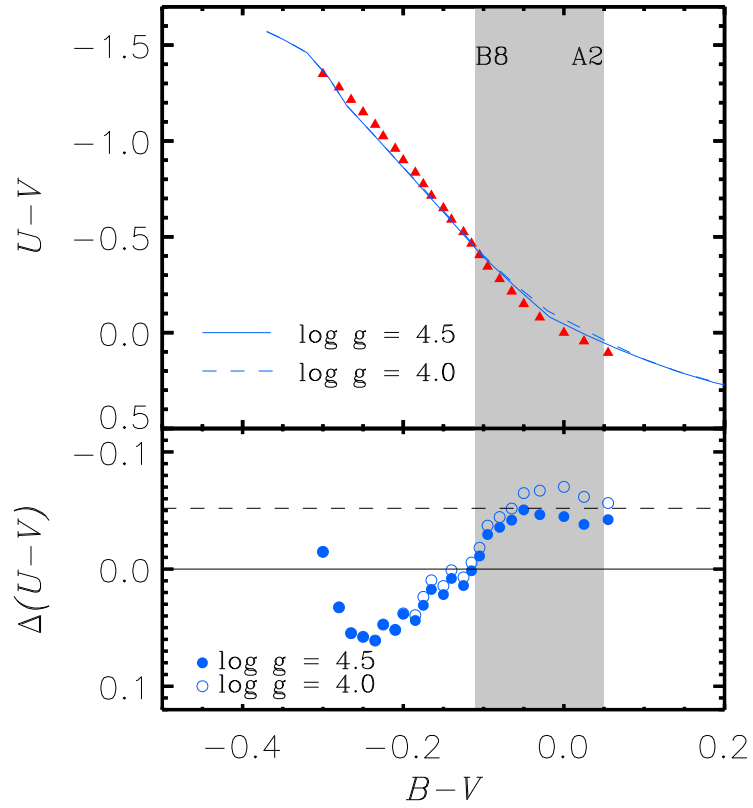
Supplementary Figure 11: **Systematic difference between two different colour scales in** $U - V$. In the top panel, triangle denotes the $(U - V, B - V)$ relation of Ref. 51. Solid and dashed line are the colour relations of Ref. 50. for $\log g = 4.5$ and 4.0, respectively. In the bottom panel, Δ means $U - V$ from Ref. 50 minus that from Ref. 51. The shaded region corresponds to the colour range of our sample stars.

Supplementary Table 1: Results of Monte-Carlo simulations

Simulation	i_{peak} (°)	σ_i (°)	α (km^{-1} s)	Confidence level (%)
Case 1	-	-	-	6.2 ± 4.0
Case 2	54	1	-	42.1 ± 13.2
Case 3	-	-	0.0006	10.7 ± 4.6
Case 4	50	2	0.0013	74.1 ± 12.8

Supplementary Table 2: Line list

Spectral lines	Spectrographs
Sr II λ4215	UVES
Cr II λ4242	UVES
Cr II λ4261	UVES
Fe I λ4235	UVES
Fe I λ4404	UVES and GIRAFFE
Fe I λ4415	UVES and GIRAFFE
Ti II λ4468	UVES and GIRAFFE
Ti II λ4488	UVES and GIRAFFE
Fe II λ4489	UVES and GIRAFFE
Fe II λ4491	UVES and GIRAFFE